Physics – Uspekhi **64** (7) 671 – 701 (2021)

REVIEWS OF TOPICAL PROBLEMS PACS numbers: 05.10.Ln, **61.46.–w**, 68.55.A–, **68.65.–k**, 73.63.Rt, **75.75.–c**

Formation and properties of metallic atomic chains and wires

A G Syromyatnikov, S V Kolesnikov, A M Saletsky, A L Klavsyuk

DOI: https://doi.org/10.3367/UFNe.2020.06.038789

Contents

1. **Introduction** **671**
2. **Formation of metallic atomic chains and wires** **672**
   2.1 Formation of atomic structures on a vicinal surface in the one-temperature regime; 2.2 Formation of atomic structures on a vicinal surface in the two-temperature regime; 2.3 Formation of one-dimensional atomic structures on the surface of metals (110) and semiconductors (001)
3. **Length distribution of atomic chains** **676**
   3.1 Equilibrium length distribution of atomic structures in the one-dimensional lattice gas model; 3.2 Solution of the rate equations; 3.3 Analysis of the distribution of atomic chain lengths with the kinetic Monte Carlo method
4. **Structural properties of atomic wires** **682**
   4.1 Determining the structure and chemical composition of atomic chains; 4.2 Structural phase transition in atomic chains of cobalt on the vicinal surface of copper
5. **Quantum effects in atomic chains** **685**
   5.1 Density of states of a two-dimensional electron gas; 5.2 Localization of surface states in single atoms and the edge state of atomic chains on a surface; 5.3 Density of states of atomic chains; 5.4 Rashba effect; 5.5 Magnetic properties of atomic wires and chains
6. **Conclusions** **698**
   References **699**

Abstract. We discuss the current state of a promising area of modern physics, the study of the physical properties of metal nanowires and atomic chains. One-dimensional nanostructures are attractive because of both the promise of their practical applications and the possibility of using them to test various theoretical models and approaches by comparing theoretical results with experimental data. We describe experimental conditions under which metal nanowires form on metal and semiconductor surfaces. We give special attention to theoretical models describing the scenario of nanowire growth on various surfaces. We analyze the main experimentally determined factors that affect the distribution of nanowire lengths. We show that the distribution of nanowire lengths on metal and semiconductor surfaces depends not only on external parameters but also on the formation time. We consider the magnetic properties of finite-length atomic chains located on the surfaces of metal and semiconductor crystals. We demonstrate a correlation among the structural, electronic, and magnetic properties of nanowires. We elucidate the effect that nanowires exert on the electronic properties of the surface on which they form. The nature of edge states is explained. The electron states of nanowire atoms are shown to be sensitive to the nanowire length. We discuss the Rashba effect for metal nanowires on a semiconductor surface and analyze how the exchange energy between atoms and the magnetic anisotropy energy affect the macroscopic characteristics of nanowires, such as their critical temperature and the time of spontaneous magnetization reversal.

Keywords: atomic wire, metallic chain, quantum conductivity, Rashba effect, nanomagnetism, spintronics, edge state, epitaxial growth

A G Syromyatnikov [(1,2,a)], **S V Kolesnikov** [(1,b)], **A M Saletsky** [(1)], **A L Klavsyuk** [(1,c)]
[(1)] Lomonosov Moscow State University, Physics Department, Leninskie gory 1, str. 2, 119991 Moscow, Russian Federation
[(2)] Semenov Federal Research Center for Chemical Physics, Russian Academy of Sciences, ul. Kosygina 4, 119991 Moscow, Russian Federation
E-mail: [(a)] ag.syromyatnikov@physics.msu.ru, [(b)] kolesnikov@physics.msu.ru, [(c)] klavsyuk@physics.msu.ru

Received 10 May 2020, revised 11 June 2020
Uspekhi Fizicheskikh Nauk **191** (7) 705 – 737 (2021)
Translated by S Alekseev

1. Introduction

Designing structures with new physical properties is one of the fundamental tasks of technology, aiming at extending the applicability limits of currently existing materials. The key concept here is the decrease in size to the limit where quantum effects start exerting a significant influence on the electronic and magnetic properties. An example of such structures is provided by metallic atomic chains (two or more interacting atoms arranged in a line) and wires (infinite atomic chains or chains long enough for the edge effects to be ignored) on the surface of metals, semiconductors, and insulators [1–25]. This is why special attention has been devoted recently to the study of properties of metallic atomic chains and wires. Revealing new physical properties in one-dimensional atomic structures allows producing new electronic devices. Such properties comprise quantized conductance [26, 27], edge electron states [28], spin and electron density waves [29], and the gigantic

Rashba effect [30]. Therefore, one of the most topical problems in modern physics consists in designing metallic atomic chains and wires with controlled properties.

The study of the processes of formation of one-dimensional atomic structures is necessary for controlling and manipulating their electronic and magnetic properties by selecting suitable experimental conditions. Despite a large number of studies devoted to the growth processes of one-dimensional structures, no general approach to the solution to this problem has been worked out so far. Because the formation of atomic one-dimensional structures and their properties is determined by the complicated character of interatomic interaction, difficulties are encountered in studying the processes of formation of atomic chains and wires. In providing a detailed description of such systems, essential help is provided by theoretical methods related to computer modeling, especially in view of the tremendous progress in computer modeling achieved recently due to the appearance of powerful computation facilities. Supercomputers have paved the way to complicated models describing realistic interatomic interactions in low-dimension systems, allowing in-depth studies of self-organization processes in one-dimensional structures.

Despite the progress in methods for studying one-dimensional structures, there are numerous unsolved problems. One of them is the analysis of the length distribution of epitaxially grown one-dimensional atomic structures. Among the various theoretical models [31–37] proposed for describing the length distribution of one-dimensional atomic structures, none attains quantitative agreement with experiment [31]. Another problem is to establish the structure of metallic atomic chains and wires on the surface of semiconductors. Here, the experimental methods do not allow determining the chemical composition of atomic structures, while theoretical approaches do not allow unambiguously determining the structure of chains and wires that form in experiment. Also of importance is the study of the thermodynamic properties of metallic atomic chains and wires. Knowledge of their behavior under changes in temperature is necessary for constructing devices and tools in the future, because it determines the applicability limits of the produced structures. Only recently did some papers appear in which the kinetic Monte Carlo method (KMCM) is used to estimate the lifetime of atomic chains [38–40].

In the last decade, spintronics has become one of the most promising directions of technological development. An intriguing question here is the following: can atomic chains and wires be used for information storage? Interest in the use of one-dimensional atomic structures as memory elements is primarily related to the possibility of their high-density arrangement on the surface of a crystal. It is therefore necessary to study the magnetic and electronic properties of one-dimensional atomic structures. In passing to the atomic scale, the leading role starts being played by the quantum properties of the considered objects, which entails obvious difficulties in experimental studies of their magnetic and electronic properties. As regards the theory, despite some degree of success in studying these problems, this field overall is still far from a comprehensive understanding of the nature and mechanisms of the relevant phenomena. One of the causes is the necessity to take various interaction types into account in detail, which, due to their nonlocality, is very laborious for both the analytic theory and numerical analysis. This is why in this review we give special attention to theoretical approaches to studying the electronic and magnetic properties of metallic chains and wires.

In this review, we describe structural, electronic, and magnetic properties of atomic chains and wires. We discuss the main theoretical models describing how these structures are formed. Based on a comparison of experimental and theoretical results, we analyze and discuss advantages and drawbacks of various theoretical approaches to the study of properties of atomic chains and wires.

2. Formation of metallic atomic chains and wires

Currently, atomic chains can only be produced with the help of a scanning tunneling microscope (STM) [1–3] and epitaxial growth. As an example, Fig. 1a shows atomic chains of copper nitride produced with the help of an STM. Manipulating atoms with an STM requires considerable effort and is time consuming, and therefore atomic structures produced in this way are hardly reproducible on an industrial scale. Hence, self-organization of atoms epitaxially sputtered on a surface is currently one of the main strategies to form metallic atomic chains and wires. Although epitaxial growth of one-dimensional structures has been investigated for many years, the role of many atomic processes involved in the formation of these structures became clear only recently. This was due to progress in experimental methods and the appearance of powerful computing systems that allow complicated models to be considered. The totality of both theoretical and experimental methods facilitates obtaining deeper insights into self-organization processes and finding optimum conditions for the growth of metallic atomic chains and wires.

In recent years, many epitaxial systems have been designed and investigated where one-dimensional atomic chains and wires form (Fig. 1b–d). They are metallic vicinal stepped surfaces [4–9] and metal [10–13] and semiconductor [14–25] surfaces with low Miller indices.

2.1 Formation of atomic structures on a vicinal surface in the one-temperature regime

Any surface can be considered vicinal, because even the most thorough treatment of the surface of a single crystal with low Miller indices leaves a certain number of steps on the surface.

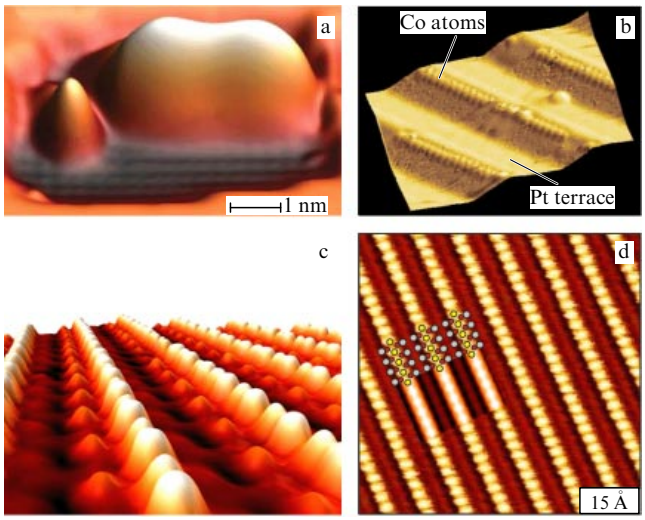

Figure 1. STM images of various one-dimensional atomic structures: (a) nitride copper wire on a Cu(100) surface [1], (b) Co wire on a Pt(997) surface [9], (c) Pt wire on a Ge(001) surface [23], (d) Co oxide wire on an Ir(100) surface [12].

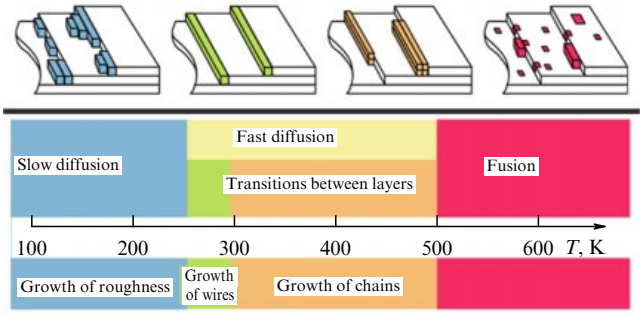

Figure 2. Formation of various Co nanostructures on a Pt(997) surface at different substrate temperatures [5, 47].

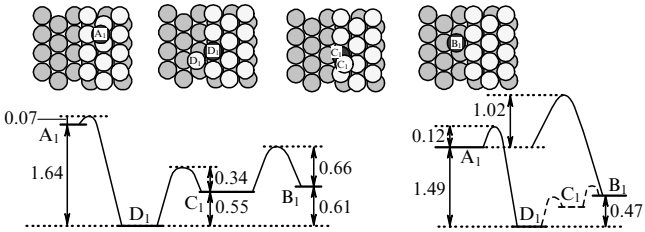

Figure 3. First phase of wire formation at the edge of a copper step: top view (left) and energy diagrams for iron (bottom left) and cobalt (bottom right). White and gray dots, respectively, denote copper atoms on the top layer and on the next layer; black dots are adatoms. Relative energies and activation energies for transitions between states are expressed in eV and are shown next to the vertical arrows [57].

The steps occur due to the mosaic structure of the crystal or because of the limited precision in orienting the crystal prior to and in the course of its sawing and polishing. For metal and semiconductor surfaces, the mean distance between steps can be as much as 500 nm, and the spread of inter-step distances around the mean value can lead to the appearance of terraces several micrometers in width on the surface. In what follows, we consider $(m, m, m+2)$ and $(m, m, m-2)$ type surfaces with small values of the index m; they are stepped surfaces with (111) terraces of m rows of atoms. Such surfaces with small values of m have narrow terraces, and for most metals the diffusion barrier for hops of atoms over a (111) surface is equal to a few dozen millielectronvolts [41–45]. On such surfaces, nanostructure growth occurs near the steps, and their geometry strongly depends on their formation temperature.

As an example, Fig. 2 shows nanostructures of cobalt formed on a Pt(997) surface at different temperatures. Because the diffusion barrier for the hop of a Co atom over the terrace is low, this atom has enough time to approach the step before the next Co atom is sputtered. The probability of hopping away from the step for Co atoms is low, because the diffusion barrier for this event exceeds 1 eV. The Co atoms then travel randomly along the step. When two Co atoms meet near the step, a dimer forms, which then becomes a center for nanostructure growth. The number of growth centers and the subsequent evolution of the system depends on the deposition rate, the surface coverage, the temperature, and the magnitude of the diffusion barrier for a single atom along the step. Hence, the main factor determining the type of forming nanostructures is the diffusion rate of Co atoms along the edge of the step. For example, at a temperature below 250 K, the diffusion rate along the step edge is low, which leads to the growth of roughness near it. In the temperature range 250–290 K, Co adatoms move along the step vigorously enough for atomic chains and wires to form. Upon a further increase in temperature, diffusion transitions between layers activate, and, hence, instead of one-atom-thick chains, wires several atoms in thickness form. At temperatures above 500 K, the Co atoms are immersed into the surface, which means fusion of the metals. As can be seen from Fig. 2, atomic wires form only in a narrow temperature range. It was established experimentally that the lower boundary of this range is 175 K for Cu and 250 K for Ag, Co, and Fe on a Pt(997) surface [46]. The upper boundary is limited by room temperature.

Another important parameter of epitaxial nanostructure growth on a surface is the coverage: the ratio of the number of deposited atoms to the number of atoms contained in one surface monolayer (ML). We discuss the effect of this parameter with the example of depositing cobalt on the vicinal surface of copper at room temperature. At low values of the coverage, of the order of 0.1 ML, two main processes are observed on the surface. First, the terrace boundaries are decorated with residual cobalt on both the higher and the lower sides of the step, such that the terrace edge acquires a 'broken' shape. Second, islets of mixed copper and cobalt atoms are placed continuously and irregularly along the step edge [48–50], making up a structure 5 nm in width. Similar one-dimensional knots also form when iron is deposited onto a vicinal surface of copper [51, 52]. As the coverage increases, adatoms on the terrace surface start forming two-layer islets [53]: small and irregularly shaped [54] as well as larger ones (about 4 nm in size) of a pronounced triangular shape. As the coverage increases further, the size of the islets increases [49] and then the islets merge [55, 56].

The above results of experimental work show that, for Co/Cu(111) at constant temperature, one-dimensional atomic structures can form in the shape of knots near the step. This behavior is also characteristic of the deposition of iron atoms on a vicinal surface of copper [51, 52].

The growth mechanism of one-dimensional atomic metallic structures on the vicinal surface of copper in the one-temperature regime was proposed in [57]. The formation of one-dimensional atomic structures at the step edge consists of the following processes: an atom approaching the clean boundary of the terrace (first phase) and an atom approaching an atomic structure already formed at the first phase (second phase).

In the first phase, iron and cobalt atoms behave similarly (Fig. 3). As an example, we therefore consider the behavior of an iron atom in this phase. In the first phase, an iron adatom prefers to occupy an fcc site on the surface (fcc stands for face-centered cubic), irrespective of its position on the surface (in the middle of the terrace or at the edge next to the step). The diffusion barrier for the hop of an adatom on the terrace is equal to 0.025 eV, and, therefore, if the terrace is narrow, the adatom soon arrives the vicinity of the step. At the step edge, in the case of in motion from its upper part, the adatom motion mechanism is much more complex. Instead of hopping to the lower terrace, with an energy barrier of 1 eV (Fig. 3, $A_1 \rightarrow B_1$), the iron adatom immerses into the step via exchange with a copper atom (Fig. 3, $A_1 \rightarrow D_1$), with the energy barrier equal to only 0.07 eV. The displaced copper atom then prefers to stay at the base of the step, next to the iron adatom.

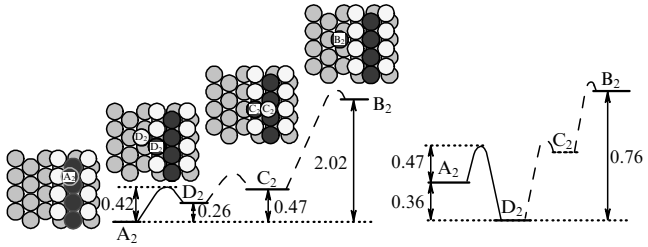

Figure 4. Second phase of wire formation at the edge of a copper step: top view (left) and energy diagrams for iron (bottom left) and cobalt (bottom right). White and gray dots, respectively, denote copper atoms on the top layer and on the next layer; black dots are adatoms. Relative energies and activation energies for transitions between states are expressed in eV and are shown next to the vertical arrows [57].

We consider an adatom located near a step on the lower terrace. The iron adatom then has to first expel a copper atom from the step (Fig. 3, $B_1 \to C_1$), overcoming a barrier equal to 0.66 eV. After that, the copper atom hops to the lower terrace, overcoming the energy barrier of 0.34 eV (Fig. 3, $C_1 \to D_1$). As a result, the final configuration is the same in both cases, irrespective of whether the iron adatom arrives at the step edge from above or from below.

As the second iron adatom approaches a terrace edge already containing an immersed iron atom (Fig. 4), it most probably continues the formation of an immersed structure two atoms in length. Subsequent iron adatoms also immerse nearby, giving rise to an immersed row of iron atoms at the edge of the step on the surface of copper.

For an iron adatom approaching the boundary of a step that already contains a row of iron atoms, it is energetically beneficial to stay above, over the atomic wire immersed near the step. As a result, additional iron adatoms placed on the vicinal surface of copper give rise to the appearance of an atomic wire made of iron on the upper boundary of the step. This is followed by an increase in the width of the wire [57, 58].

Because iron and cobalt atoms interact with a copper surface in the same way, the exchange processes occur similarly for cobalt atoms (see Fig. 3). The distance between the nearest neighbors in a copper crystal is $d_{\mathrm{Cu-Cu}} = 2.56$ Å, but is lower for the body-centered cubic (bcc) lattice of iron: $d_{\mathrm{Fe-Fe}} = 2.48$ Å. For cobalt, the distance between nearest neighbors is $d_{\mathrm{Co-Co}} = 2.51$ Å, which allows the immersed cobalt wire to embed into the surface of the copper substrate fcc lattice even better than into the iron lattice. Although the first phase (formation of an atomic wire) occurs in the same way for both iron and cobalt atoms, essential differences show up in the second phase, because the cobalt crystal has a hexagonal structure, and its (0001) surface has the same shape as the (111) surface of copper. In addition, the distance between nearest neighbors is approximately the same in the two cases, and therefore cobalt atoms immerse into the surface, thus increasing the width of the embedded cobalt chain two-fold.

As shown in Fig. 4, when an adatom moves from the lower part of the step, its final position is lower in energy than the initial one, which makes its immersion into the step possible via exchange with the atoms of the step. If cobalt atoms move to the terrace edge from above, they immerse into the step by displacing copper atoms, which results in an increase in the width of the embedded cobalt wires [57, 58].

2.2 Formation of atomic structures on a vicinal surface in the two-temperature regime

Epitaxial growth of thin metallic films and nanostructures on the surface of metals has been in the focus of interest of research groups for more than half a century; for example, growth of cobalt on a copper surface was first described in 1936 [59]. Since then, the Co/Cu(111) system has been intensely studied by various research groups [8, 48, 49, 52–56, 60, 61]. Despite this, however, it was long considered impossible to produce atomic chains of Co and Fe on the vicinal surface of copper by epitaxial growth. Indeed, as was shown both experimentally [48, 49, 52–56, 60] and theoretically [37, 57, 58, 62], the formation of atomic Co and Fe chains on the vicinal surface of copper is impossible in the one-temperature regime. But the formation of atomic Co chains has been demonstrated in the two-temperature regime [8, 61], when Co atoms were first deposited onto the vicinal surface of Cu(775) in the amount of 0.02 ML at the rate of 0.01 ML min^{-1} at 165 K. After that, the sample was heated to room temperature for some time.

The mechanism of growth of one-dimensional atomic metallic structures on the vicinal surface of copper in the two-temperature regime is as follows [58, 62]. After sputtering on the surface, Co adatoms perform random walk over the terrace, overcoming the barrier of 40 meV, until they reach the edge of the step. On a clean surface, an adatom approaching the terrace edge must overcome its repulsive barrier. The repulsive barrier for a Co adatom is much higher on the upper terrace (136 meV) than on the lower one (69 meV). This can be clearly seen from Fig. 5a, which plots the potential energy for a Co adatom on the vicinal surface of Cu(775). This is why at temperatures in the range 150–170 K the adatoms most probably approach the step from the lower side of the terrace. Only a few adatoms (two or three out of a thousand) approach the edge from above [63]. Such a difference is caused by charge redistribution on the step edge [63, 64] and leads to the interaction between an adatom and the step being different on the upper and lower terraces. For example, decreasing the electron density on the upper terrace edge reduces the screening of the direct Coulomb interaction between the Co adatom and the atoms of the step edge and hence decreases the repulsive barrier. As a result, repulsion between the adatoms and the step edge can considerably decrease the diffusion of adatoms toward the edge.

A detailed analysis of the interaction of a Co adatom with the vicinal surface of Cu(111) reveals an amusing effect [58, 62]. The chain located near the terrace edge increases the energy of the adatom interaction with the surface in the middle of the lower terrace (Fig. 5b) and, conversely, decreases it in the middle of the upper terrace (Fig. 5c). Therefore, the cobalt chain stops the diffusion of adatoms on the lower terrace and facilitates it on the upper terrace, thus playing, as it were, the role of a nanosemaphore [62] for adatoms moving over the terrace. In this case, the Co adatoms have a higher probability of approaching the step from the lower terrace and in the locations least crowded with the Co adatoms. The few Co adatoms that arrive from the side of the upper terrace can embed into the step edge due to fluctuations of its atoms caused by vacancy diffusion or via the exchange mechanism at the step edges [65]. The potential barrier for such an event is 250 meV. Two adatoms meeting on the terrace can form a dimer. The probability of this process decreases as the temperature increases and as the terrace width decreases. The first stage terminates when most of the adatoms come to the step edge.

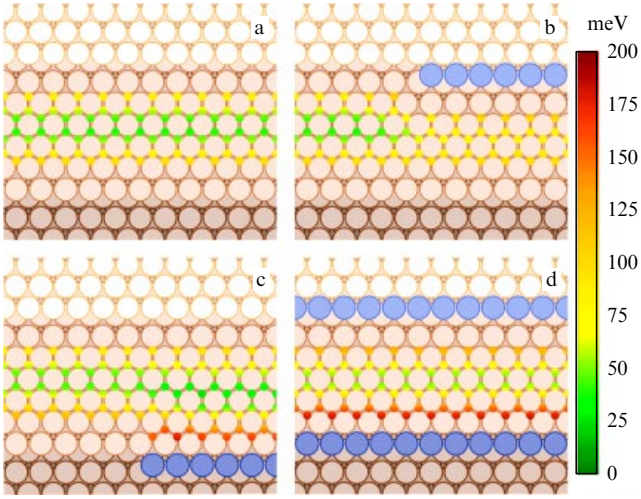

Figure 5. (Color online.) Map of the potential energy for a Co adatom on a Cu(775) vicinal surface. (a) Atomic chains of cobalt are present on the surface. (b, d) Atomic chains of cobalt are present on different terraces on the surface. (c) Clean surface [37].

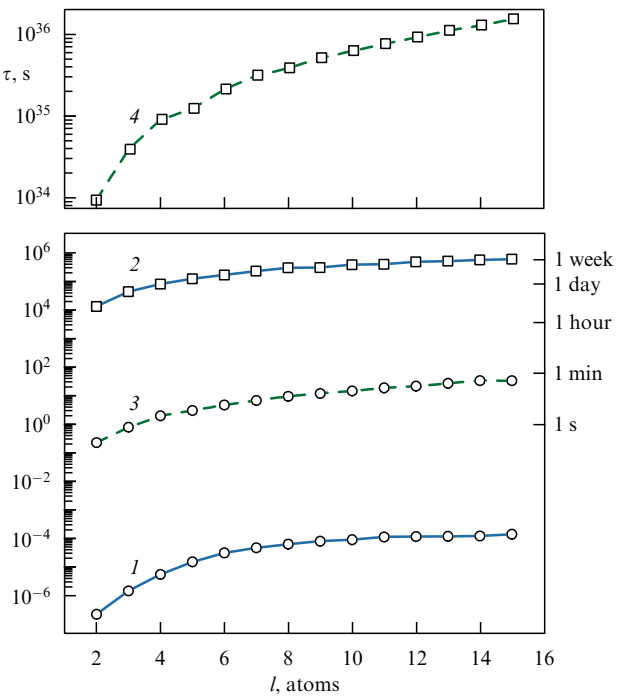

Figure 6. Mean lifetime of a chain depending on its length in systems Ag/Pt(997) (curve *1* at 160 K, curve *2* at 100 K) and Co/Cu(775) (curve *3* at 160 K, curve *4* at 100 K) [38].

At the second stage, the formation of atomic chains continues on the vicinal surface due to the coalescence of adatoms and dimers near the step. Because the diffusion barrier for a hop of a Co adatom near a 300-meV step is an order of magnitude higher than on the terrace, it follows that increasing the temperature increases the diffusion rate [8, 46]. The duration of the second stage depends on the ratio of the binding energy in the atomic chain to the temperature. The lower that ratio, the faster the atomic chains merge and the sooner equilibrium is reached. For example, a system of atomic chains of silver on a Pt(997) surface with a binding energy of 60 meV at 160 K arrives at thermodynamic equilibrium in several seconds [38]. If the temperature is decreased, then the time for the system to arrive at thermodynamic equilibrium drastically increases. As can be seen from Fig. 6, at 100 K, the Ag/Pt(997) system does not come to thermodynamic equilibrium even in the course of several days. We note that, at temperatures below 105 K, atoms of silver become less mobile near the step, and, therefore, at low temperatures atomic chains do not equilibrate within the duration of the experiment. For atomic chains of cobalt on the Cu(775) surface at temperatures above 160 K, the relaxation time is much shorter than the experiment duration time [39, 40, 66]. The second stage terminates when atomic chains and wires of different lengths form.

2.3 Formation of one-dimensional atomic structures on the surface of metals (110) and semiconductors (001)

An important factor determining nanostructure growth, besides the nature of the impurity and substrate material, the temperature, the deposition rate, and the coverage, is the symmetry of the substrate surface. We consider its impact on the growth of one-dimensional structures with the example of the unreconstructed metal surface fcc(110) [11, 51, 67, 68] and the reconstructed surface of diamond-type (001) semiconductors [19, 69–73]. On such surfaces, symmetry arguments allow epitaxial growth of one-dimensional atomic structures.

The unreconstructed fcc(110) surface of metals consists of densely packed rows of atoms placed at a distance of next-to-nearest neighbors from each other (Fig. 7a). Therefore, the diffusion of atoms over the surface occurs primarily along these rows, i.e., along the $[1\bar{1}0]$ crystallographic direction, and to a minor degree, along the perpendicular direction [001], because activation barriers for diffusion along these directions differ strongly for most metals [43]. For example, diffusion barriers for Cu/Cu(110) along $[1\bar{1}0]$ and [001] are, respectively, equal to 241 and 1020 meV [43]. Another example is given by the reconstructed surfaces of diamond-type (001) silicon and germanium, c(4×2) and p(2×2), made of a row of surface dimers [74, 76] placed in every second row, as shown in Fig. 7b. As in the case of an fcc(110) surface, diffusion of adatoms also primarily occurs along one direction. The possibility of epitaxial formation of one-dimensional atomic structures on the fcc(110) surface of metals [11, 51, 67, 68] and on the reconstructed surface of diamond-type (001) semiconductors [14–25, 75] has been confirmed experimentally. In Fig. 7c, d, we show STM images of atomic wires for Cu/Pd(110) [67] and Ir/Si(001) [75].

Besides the anisotropy of diffusion barriers for single atoms, the surfaces under consideration exhibit anisotropy of the binding energy. In the case of sputtering up to 0.10 ML, just this anisotropy, along with the temperature, the coverage, and the deposition rate, determines the conditions for the formation of atomic wires [77–81]. We consider how the ratio of the coverage Θ to the atom deposition rate F affects the formation of one-dimensional structures on the (110) surface. For small Θ/F, the mobility of atoms is low, because the time interval between the appearance of two atoms is very short, and within this short period of time the atom can only reach another atom or a defect. Thus, at the first stage, a large number of growth centers — dimers — form. Subsequently, only short chains two to three atoms in length and one to two atoms in width form. We note that, in contrast to (001) and (111) metal surfaces, the growth of dendrites is impossible on a (110) surface. Atomic chains are kinetically stabilized structures as long as the energy is insufficient for breaking

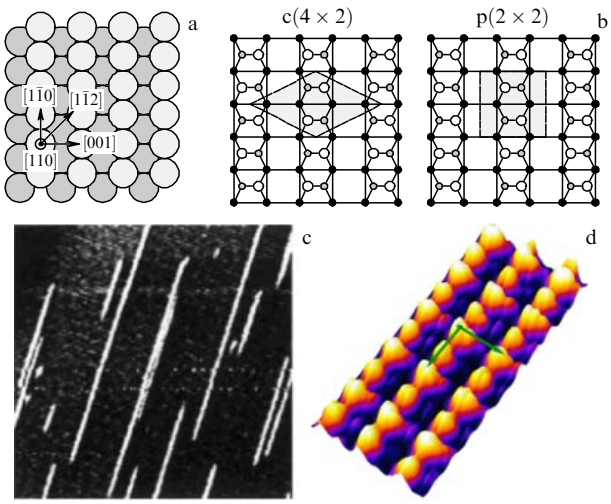

Figure 7. (a) View of an fcc(110) surface and three possible directions for the diffusion of adatoms [43]. (b) Reconstructed diamond type (001) surfaces c(4 × 2) and p(2 × 2) [74]. (c) STM image of Cu atomic wires on a Pd(110) surface [67]. (d) STM image of Ir atomic wires on an Si(001) surface [75].

the bond of an edge atom to the chain. As Θ/F increases, the number of growth centers decreases and self-organization of atomic chains occurs. A further increase in Θ/F leads to the widening of atomic chains and the formation of rectangular islets.

We discuss mechanisms whereby the binding energy anisotropy affects the shape of self-organizing structures. We let E_1 and E_2 be the binding energies of two atoms on the surface, placed along two perpendicular directions. Because of the anisotropy of the surface (Fig. 7a or b), the distance between two atoms on the surface is shorter in one direction than in the other, perpendicular, direction, and hence $E_1 \gg E_2$. As a result, for a small number N of atoms, the energetically stable configuration is given by a linear chain of atoms. If the length of the chain reaches the critical length N_{crit} (the number of atoms), the formation of a second row of atoms becomes energetically advantageous. To find the critical length N_{crit}, we consider two atomic structures: a chain $2N_{\text{crit}}$ in length and an islet N_{crit} in length and two atoms in width. The binding energy for the atomic chain is $(2N_{\text{crit}} - 1)E_1$, and that of the islet is $(2N_{\text{crit}} - 2)E_1 + N_{\text{crit}}E_2$. Equating these two, we can estimate the critical length of the atomic chain as $N_{\text{crit}} = E_1/E_2$. For Cu/Cu(110), for example, $E_1 = 0.3$ eV and $E_2 = 0.03$ eV [78], and $N_{\text{crit}} = 10$. As a result, for low concentrations, atomic chains up to 10 atoms in length form, and at higher concentrations, rectangular elongated islets form.

3. Length distribution of atomic chains

One-dimensional atomic structures are attractive as regards the design of new modern electronic devices. For their use in electronic devices, it is desirable that they have the same length and be well ordered systematically. This is why one-dimensional structures and their size distribution are investigated both experimentally and theoretically. In experiment, the length distribution of atomic chains is most commonly studied at low temperatures with the help of an STM [8, 20, 31]. Theoretical studies and analyses of the length distribution

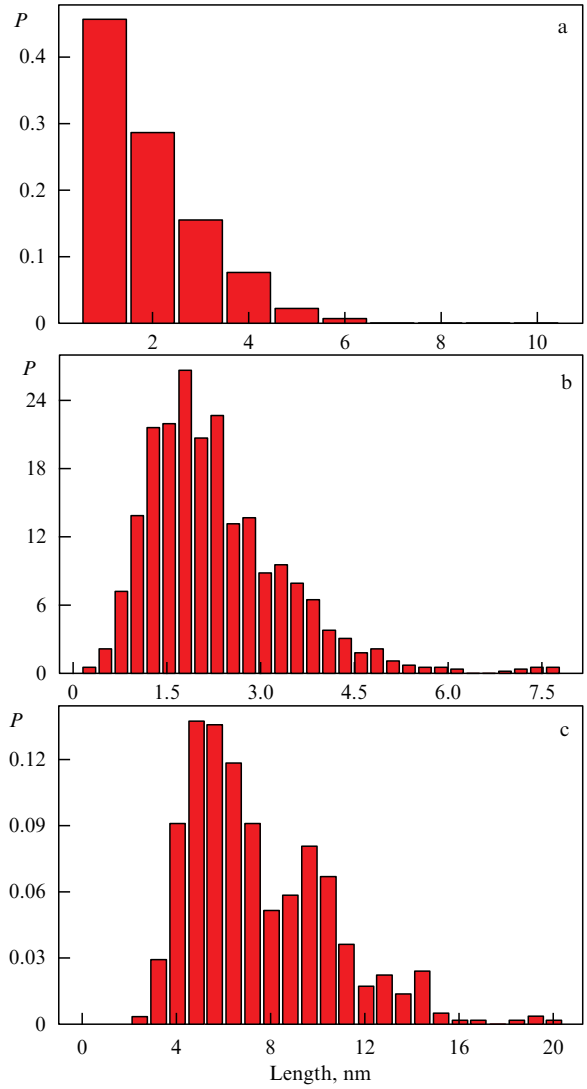

Figure 8. Three characteristic distributions of atomic chain lengths: (a) $Co_{0.33}Ni_{0.67}O_2$/Ir(001) [12], (b) Ag/Pt(997) [31], (c) Ir/Ge(001) [20].

of one-dimensional atomic structures are performed for epitaxially grown systems. Currently, three main types of length distributions for chains are identified (Fig. 8). Those of the first type have a maximum corresponding to one structural element, and their distribution function decreases as the length of the one-dimensional structure increases. In Fig. 8a, we show a distribution of this type, observed for $Co_{0.33}Ni_{0.67}O_2$/Ir(001) chains. Distributions of the second type have one pronounced maximum (Fig. 8b). Distributions of the third type are characterized by two or more maxima, with the height of the subsequent maxima greatly reduced. In Fig. 8c, we show the distribution for Ir/Ge(001) chains as an example.

Modeling the process of growth of atomic chains and wires, as well as studying the effect of external factors on their length distribution, is of primary importance for understanding the physical properties of irreversible systems far from equilibrium, and also for assessing the possibility of controlling the morphology of the emerging structures. There are three approaches to the theoretical analysis of the length distribution of atomic chains and wires. In the first, in the framework of thermodynamics with the use of a one-

dimensional lattice gas model, an analytic expression is obtained for the length distribution function of one-dimensional structures [31, 32]. The second approach is based on solving the rate equations, which are solved analytically by scaling functions [82]. The third approach is based on the use of the KMCM [37–39, 83–85]. Currently, however, the length distribution of one-dimensional structures is most often studied by combining two approaches. In particular, rate equations are solved, after which the solution is compared with KMCM results [33, 35, 86–91]. The approaches named above have yielded many important and interesting results which sometimes contradict each other. In what follows, we give a detailed description of the use of these approaches in theoretical studies of the length distribution of atomic chains and wires.

3.1 Equilibrium length distribution of atomic structures in the one-dimensional lattice gas model

To derive the equilibrium length distribution function for one-dimensional atomic structures, we consider the model of a one-dimensional lattice gas [31, 32]. We consider a row of n sites along which the atoms can be located. Each of the n sites can be either occupied or free. We restrict ourself to the interaction between neighboring atoms. The atomic chain in this model is a sequence of occupied sites, limited by unoccupied sites on both ends. The equilibrium distribution function can be found in the canonical ensemble framework, i.e., assuming the number of occupied sites n_1 to be constant.

We first find the number of atomic chains. The partition function of the system can be written as [32]

$$Z = \sum_q \frac{n}{q}\, g_1 g_2 \exp\left(-\frac{E}{k_\mathrm{B}T}\right), \tag{1}$$

where g_1 and g_2 are the degeneracy factors, q is the number of chains, related to the energy as

$$E = -\epsilon\,(n_1 - q)\,, \tag{2}$$

and ϵ is the binding energy.

Summation in expression (1) ranges all possible values of q. The minus sign in front of the right-hand side in (2) implies that the neighboring atoms are attracted for positive ϵ. The g_1 factor is equal to the number of arrangements of n_1 occupied sites among the q chains,

$$g_1 = \frac{(n_1 - 1)!}{(n_1 - q)!(q-1)!}\,, \tag{3}$$

and g_2 is equal to the number of arrangements of $n_0 = n - n_1$ unoccupied sites in the q voids between the chains:

$$g_2 = \frac{(n_0 - 1)!}{(n_0 - q)!(q-1)!}\,. \tag{4}$$

The factor n in (1) is the number of possible configurations, and $1/q$ is introduced for correction for the superfluous configurations occurring in the case of periodic boundary conditions. Depending on which of the q clusters is the first one, we can divide the collection of ng_1g_2 configurations into q subcollections, which are identical.

To find q, we use the asymptotic method in which the partition function is replaced with its greatest summand. Solving the resultant equation in the thermodynamic limit $n \to \infty$, we obtain the number of chains as

$$q = \frac{\sqrt{n^2 + 4n_0n_1\big(\exp(\epsilon/k_\mathrm{B}T) - 1\big)} - n}{2\big(\exp(\epsilon/k_\mathrm{B}T) - 1\big)}\,. \tag{5}$$

From the number of chains and the temperature of the system, we find the binding energy

$$\epsilon = k_\mathrm{B}T \ln \frac{(n_1 - q)(n - n_1 - q)}{q^2}\,. \tag{6}$$

To derive the distribution function of the chain lengths, we rewrite the partition function using other variables. We let q_l denote the number of chains of length l. Then each collection of chains $\{q_k\}$ must satisfy the conditions

$$n_1 = \sum_{k=1}^{\infty} k q_k\,, \quad q = \sum_{k=1}^{\infty} q_k\,. \tag{7}$$

Substituting these into (2), we express the total energy of the collection of chains $\{q_k\}$ as

$$E = -\epsilon \sum_{k=1}^{\infty} (k-1) q_k\,. \tag{8}$$

We next find the degeneracy factor for the collection $\{q_k\}$. We first suppose that the chains have different lengths. With the periodic boundary conditions, there are n ways to choose the position of the first cluster. By definition, each chain is bounded by two unoccupied sites, which leaves $n_0 - 1 = n - n_1 - 1$ positions for the remaining $q - 1$ chains. There are $(n_0 - 1)!/(n_0 - q)!$ possibilities to arrange these chains. But because all chains of the same length are indistinguishable, we must introduce a correction for the number of translations inside each group of chains of length k. We can then write the degeneration factor for the collection of chains $\{q_k\}$ as

$$g_3 = \frac{n\big(\sum_{k=1}^{\infty} k q_k - 1\big)!}{\big(n - \sum_{k=1}^{\infty}(k+1)q_k\big)! \prod_{k=1}^{\infty} q_k!}\,, \tag{9}$$

and the partition function as

$$Z = \sum_{\{q_k\}} g_3 \exp\left(-\frac{E}{k_\mathrm{B}T}\right), \tag{10}$$

where summation ranges all collections of clusters satisfying conditions (7). To find the number of chains of length l, we use the Lagrange method to find an extremum of the natural logarithm of the partition function. We can then write

$$\frac{\partial}{\partial q_l}\Bigg[\ln g_3\big(\{q_k\}\big) - \frac{E\big(\{q_k\}\big)}{k_\mathrm{B}T} + \lambda_1\left(n_1 - \sum_{k=1}^{\infty} k q_k\right) + \lambda_2\left(q - \sum_{k=1}^{\infty} q_k\right)\Bigg] = 0\,, \tag{11}$$

where the expression in square brackets is a Lagrange function constructed from (10) and constraint equations (7), and λ_1 and λ_2 are Lagrange multipliers. Using expressions (8) and (9), we can rewrite system (11) as

$$q_l = S_1^l S_2\,, \tag{12}$$

where

$$S_1 = \frac{n - n_1 - q}{n - n_1 - 1} \exp\left(-\frac{\epsilon}{k_B T}\right) \exp(-\lambda_1) \tag{13}$$

and

$$S_2 = (n - n_1 - q) \exp\left(-\frac{\epsilon}{k_B T}\right) \exp(-\lambda_2) \tag{14}$$

are constants independent of l. Substituting (12) into (7) and solving for S_1 and S_2, we obtain

$$S_1 = 1 - \frac{q}{n_1}, \quad S_2 = \frac{q^2}{n_1 - q}. \tag{15}$$

With these relations, expression (12) for the size distribution of chains becomes

$$q_l = \frac{q^2}{n_1}\left(1 - \frac{q}{n_1}\right)^{l-1}. \tag{16}$$

Dividing Eqn (16) by the total number of chains q, we finally obtain the distribution function

$$F(l) = \frac{q}{n_1}\left(1 - \frac{q}{n_1}\right)^{l-1}. \tag{17}$$

The distribution function of chain lengths (17) well describes distributions of the first type, shown in Fig. 8, but poorly describes other distribution types. It has been hypothesized that the one-dimensional lattice gas model does not take the strong deformation of short chains into account [31] (although, as we show below, this is not the case). Nevertheless, the one-dimensional lattice gas model is used to find the binding energy ϵ. The experimental distribution of lengths of atomic chains is approximated by theoretical distribution function (17), and the number of chains q is then determined. Next, Eqn (6) is used to find the binding energy of atomic chains [8, 31]. The binding energies obtained for some systems in this approach differ significantly from those calculated in the framework of the density functional theory. For example, for Co/Cu(775), the binding energy is 0.13 eV [8], whereas the density functional theory gives 0.56 eV [8, 31]. Thus, the model of a one-dimensional lattice gas describes not all one-dimensional atomic structures, which necessitates developing other approaches to the analysis of length distributions of atomic one-dimensional structures.

3.2 Solution of the rate equations

Another approach to the analysis of length distributions of atomic one-dimensional structures amounts to solving rate equations with the use of scaling functions. This approach is one of the best for studying the formation of atomic structures at the stage preceding their coalescence [92– 95]. One of the most interesting properties of such distributions is so-called scaling [92 –96].

The growth of one-dimensional islets (atomic chains and wires) on the surface can be divided into two stages: transient and steady-state. At the first stage, the density of single adatoms N_1 increases due to the deposition of new atoms, but, at the second stage, it is compensated by the adatoms being adjoined to islets. In the transient regime, the density of single adatoms increases as $N_1 \approx Ft$, which leads to the

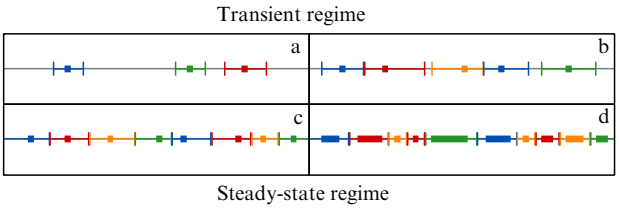

Figure 9. (Color online.) (a) Diagram of depletion zones (thin color lines) around newly formed one-dimensional islets (thick lines of the same color) in the transient regime, their (b) growth, (c) overlap, and (d) transformation into capture zones in the steady-state regime. Color coding corresponds to different growth centers.

appearance of islets located at some distance from each other (Fig. 9a). The islets are surrounded by depletion bands, and therefore the number of single adatoms N_1 decreases due to the their adjoining the islets in these bands. The radii of depletion zones increase with time as $\sqrt{\tau}$, where τ is the time from the nucleation start instant (Fig. 9b). With time, depletion zones overlap and cover the entire surface. At that instant, the depletion zones turn into capture zones that surround each newly formed islet (Fig. 9c). In the subsequent stable regime, most of the sputtered atoms join the islets, mainly those in the center of the corresponding capture zone (Fig. 9d). Thus, knowing the parameters of capture zones allows estimating the islet growth rate [97–99].

We consider the case where the islets are immobile. For simplicity, we introduce the islet critical size i, upon attaining which the islet becomes stable, which means that an atom cannot detach from an islet consisting of $i + 1$ or more atoms. The density of stable islets is $N_{\text{isl}} = \sum_{s>i} N_s$, where N_s is the density of islets made of s atoms. We introduce the surface coverage parameter $\Theta = \sum_{s \geqslant i} sN_s = Ft$, where t is the deposition time and F is the deposition rate. We consider the rate equations for the formation of mean-density islets. The nucleation rate is $K_{\text{nuc}} = \sigma_i h N_1 N_i$ (where h is the eigenfrequency of adatom hops, σ_i is the capture coefficient describing the probability of capture of wandering adatoms by unstable islets of size i, and N_1 is the density of single atoms). To simplify the analysis, we disregard the possibility of depositing an adatom from above or in the immediate vicinity of the islet. The rate of aggregation (of the capture of adatoms by islets) is $K_{\text{agg}} = \langle\sigma\rangle h N_1 N_{\text{isl}}$, where $\langle\sigma\rangle$ is the mean capture coefficient for stable islets. The rate equations for the mean densities of adatoms and islets take the form [100–102]

$$\frac{\mathrm{d}N_1}{\mathrm{d}t} \approx F(1 - \Theta) - (i + 1)K_{\text{nuc}} - K_{\text{agg}}, \tag{18}$$

$$\frac{\mathrm{d}N_{\text{isl}}}{\mathrm{d}t} \approx K_{\text{nuc}}, \tag{19}$$

$$N_i \approx c_i \exp(-\beta E_i)(N_1)^i, \tag{20}$$

where (20) describes the density of critical clusters [103], with c_i being the number of states of critical clusters with the minimal energy $E_i < 0$, and $\beta = 1/k_B T$. Integrating this system yields two different regimes: transient and steady-state. As was qualitatively shown above, $(\mathrm{d}/\mathrm{d}t)N_1 \approx F$ in the transient regime, which gives

$N_1 \approx Ft = \Theta$, and $((\mathrm{d}/\mathrm{d}t)N_1 \approx F(1-\Theta) - K_{\mathrm{agg}} \approx 0$ and $N_1 \approx F(1-\Theta)/(\langle\sigma\rangle hN_{\mathrm{isl}}) \approx F/(\langle\sigma\rangle hN_{\mathrm{isl}})$ in the steady-state regime. The transition from one regime to another occurs at $\Theta^* \sim \exp[\beta E_i/(i+3)](h/F)^{-2/(i+3)}$.

Assuming that the capture coefficients σ_i are independent of Θ, it can be shown [100–102, 104–106] that

$$N_{\mathrm{isl}} \sim \Theta^{i+2} \exp(-\beta E_i)\left(\frac{h}{F}\right) \tag{21}$$

in the transient regime,

$$N^*_{\mathrm{isl}} \sim \exp\left(-\frac{\beta E_i}{i+3}\right)\left(\frac{h}{F}\right)^{-\chi^*} \tag{22}$$

at the crossover where $\Theta \approx \Theta^*$, and

$$N_{\mathrm{isl}} \sim \Theta^{1/(i+2)} \exp\left(-\frac{\beta E_i}{i+2}\right)\left(\frac{h}{F}\right)^{-\chi} \tag{23}$$

for Θ close to 1.

The scaling exponents χ and χ^* satisfy the conditions $\chi = i/(i+2)$ and $\chi^* = (i+1)/(i+3)$, whence

$$\chi^* - \chi = \frac{2}{(i+2)(i+3)} > 0\,,$$

and therefore $N_{\mathrm{isl}} > N^*_{\mathrm{isl}}$ in the steady-state regime. This indicates that, in the limit as $h/F \to \infty$, nucleation occurs in the steady-state regime. The same is also true for finite h/F, especially for small i.

We consider the scaling of the islet size distribution. At a large ratio of the adatom diffusion coefficient D to the deposition flux F, $D/F \to \infty$, the expected form of the density distribution of islets consisting of s atoms at instant t has the form

$$n(x, \langle s\rangle, \Theta) = \frac{\Theta}{\langle s\rangle^2} f(x)\,, \quad x = \frac{s}{\langle s\rangle} \tag{24}$$

for all times except very short ones. Here, $\langle s\rangle$ and Θ are the time-dependent mean size of an islet and the coverage, and $f(x)$ is a universal scaling function independent of both $\langle s\rangle$ and Θ. Because the surface density of islets N is related to $\langle s\rangle$ and Θ as $N\langle s\rangle \cong \Theta$, the scaling function must satisfy two normalization conditions:

$$\int_0^\infty f(x)\,\mathrm{d}x = \int_0^\infty x f(x)\,\mathrm{d}x = 1\,. \tag{25}$$

The characteristic form of the scaling function for different values of Θ is shown in Fig. 10. In modeling, the growth of islets is always assumed irreversible or having a time-dependent critical islet size. The irreversible character of growth leads to pronounced asymmetry of the distribution function shape, in contrast to models where the decay of islets is allowed. Reversible growth, on the contrary, is characterized by distribution functions close to the normal distribution in shape [93].

In studying the growth of islets, the heterogeneous irreversible growth model is typically considered [107, 108]. As an example, we discuss a simple model where islets A_s grow due to mobile adatoms A_1 in accordance with the pattern $A_s + A_1 \to A_{s+1}, s \geqslant 1$, which is described by a set of rate

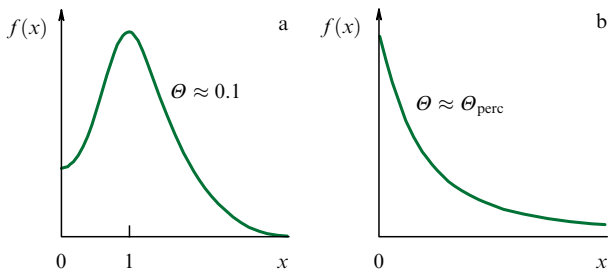

Figure 10. Scaling functions for the size distribution of islets $f(x)$ depending on the scaled islet size $x = s/\langle s\rangle$ (a) at a low coverage Θ and (b) near the percolation threshold. Adapted from [93].

equations for the surface concentration of islets N_s:

$$\begin{aligned} \frac{\mathrm{d}N_1}{\mathrm{d}t} &= F - 2D\sigma_1 N_1^2 - DN_1 \sum_{s\geqslant 2} \sigma_s N_s\,, \\ \frac{\mathrm{d}N_s}{\mathrm{d}t} &= DN_1(\sigma_{s-1}N_{s-1} - \sigma_s N_s)\,, \quad s \geqslant 2\,, \end{aligned} \tag{26}$$

where σ_s is a capture coefficient dependent on the cluster size and introduced as

$$\sigma_s(\Theta) = \alpha(\Theta)(a + s - 1)\,, \quad s \geqslant 1\,, \tag{27}$$

where $\alpha(\Theta)$ is a suitable function that ensures agreement with the results of numerical modeling [99, 109, 110] at large s. We note that σ is a linear function not for all islet sizes [99, 109–112], and therefore this model may not ensure full correspondence with real experiment. However, choosing σ in this way allows obtaining an exact analytic solution in the form of a modified beta distribution depending on two parameters, a and p, and satisfying condition (25).

According to [113, 114], rate equations (26) can be simplified by introducing a time-dependent variable z as

$$\frac{\mathrm{d}z}{\mathrm{d}t} = DN_1\alpha\,, \quad z(t=0) = 0\,, \tag{28}$$

which leads to linearizing the equations. We assume a power-law dependence

$$\alpha(\Theta) = c\Theta^p\,, \tag{29}$$

with $c > 0$ and $p > -1$. Solving the system of equations by the method of generating functions, we obtain a discrete distribution of islet sizes in the form [108]

$$N_{s+1}(\langle s\rangle, \Theta) = \frac{\Theta}{\langle s\rangle^2}\,\frac{(p+1)b^{p+1}}{a\langle s\rangle^p}\,\frac{B(s, a-p)}{B(s,a)} \times I_{1-b/\langle s\rangle}(s, a-p)\,, \tag{30}$$

where

$$b = \frac{(a+1)(p+1)}{p+2}\,, \tag{31}$$

$$I_y(s,q) = \frac{1}{B(s,q)}\int_0^y t^{s-1}(1-t)^{q-1}\,\mathrm{d}t \tag{32}$$

is a regularized incomplete beta function,

$$B(s,q) = \frac{\Gamma(s)\Gamma(q)}{\Gamma(s+q)} \tag{33}$$

is the beta function, and $\Gamma(s)$ is the gamma function. The obtained distribution (30) depends on two parameters, a and p, which have different physical meanings depending on the system. The p parameter determines the dependence of the capture coefficient σ_s on the coverage Θ and is equal to zero when they are independent. In particular, in the case of a homogeneous growth of a two-dimensional islet, the a parameter is referred to as the rate of dimerization [108].

Using the asymptotic form of the incomplete beta function as $s \to \infty$, $\langle s \rangle \to \infty$ for finite values of b and $a - p$, we can write

$$I_{1-b/\langle s \rangle}(s, a-p) \cong \gamma\left(\frac{bs}{\langle s \rangle}, a-p\right), \tag{34}$$

where

$$\gamma(y,a) = \frac{1}{\Gamma(a)} \int_y^\infty t^{a-1} \exp(-t)\, \mathrm{d}t \tag{35}$$

is the regularized incomplete gamma function. Also using the property of the gamma and beta functions,

$$\frac{B(s,a-p)}{B(s,a)} \cong s^p \frac{\Gamma(a-p)}{\Gamma(a)}, \quad s \gg a, \tag{36}$$

we obtain a continual approximation for discrete distribution (30) in form (24) with the scaling function

$$f(x) = (p+1)\, p^{b+1} \frac{\Gamma(a-p)}{\Gamma(a+1)} x^p \gamma(bx, a-p). \tag{37}$$

We see that scaling function (37) is universal, i.e., is independent of both $\langle s \rangle$ and Θ. Substitution shows that this function satisfies normalization condition (25) for any a and p. In Fig. 11, we compare numerical solutions of rate equations (26) with the dependence $f(x)$ satisfying Eqns (27) and (29) for the parameter values $a = 2$, $p = 0.5$, $c = 10$, and $D/F = 10^5$.

The scaling hypothesis also enjoys successful use in describing the growth of one-dimensional structures on a surface in numerical modeling via the KMCM [35, 88, 90, 115, 116] and in real experiments for various systems [86, 89, 117, 118].

For example, the growth of Ga [86] and In [89] chains on an Si(100) surface was investigated experimentally using the STM and numerically via the KMCM. A distinctive feature of the Si(100) surface is the existence of defects of various types [119]. It has been shown that the existence of diverse defects does not have a strong effect on the results, and therefore some types of defects — those that are not nucleation centers — can be disregarded. For Ga deposited with the deposition rate $F = 10^{-3}$ ML s^{-1} at room temperature, gallium wires form along the direction perpendicular to the silicon dimers paving the surface. Calculations done for six different values of the coverage parameter (ranging from 0.066 to 0.131 ML) show that the distributions of chain lengths overlap when constructed in normalized coordinates, thereby confirming the scaling theory. Similar results are also observed for In/Si(100).

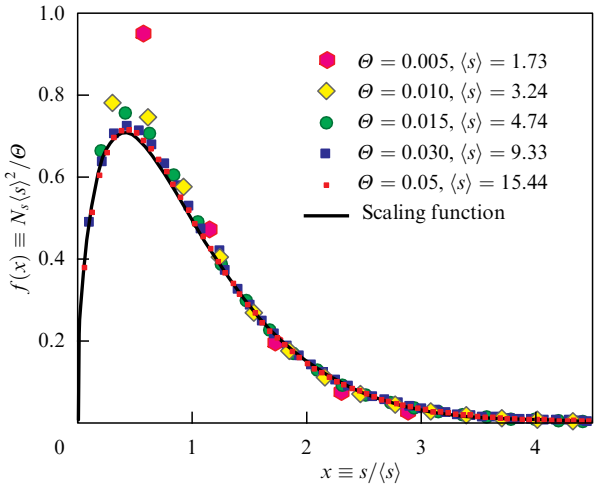

Figure 11. (Color online.) Comparison of numerical solutions of the rate equations with the capture coefficients linear in islet size, with $a = 2$, $p = 0.5$, $c = 10$, and $D/F = 10^5$, at different values of the order parameter Θ. The analytic function $f(x)$ is shown with a solid line. Adapted from [108].

Of special interest are the results of calculations that reveal the experimental conditions under which the distribution function of atomic chain lengths changes from a monotonically decreasing function (Fig. 8a) to a function with a pronounced maximum (Fig. 8b).

For example, at the critical concentration of defects equal to 0.0025 ML, the distribution function of chain sizes changes from a unimodal to a monotonically decreasing form [36]. The possibility of the distribution changing from the unimodal to the monotonically decreasing form as the temperature or the coverage of the sputtered atoms varies was shown in [87]. It was claimed in [33] that, at thermodynamic equilibrium, the distribution function of lengths of one-dimensional atomic structures has a maximum when the dependence of the binding energy of chains on length has a positive curvature. However, with this dependence of the binding energy, the atoms must repel each other in short chains and attract each other in long chains. As a result, dimers should not form, because atoms repel. But dimers are growth centers for one-dimensional structures.

Thus, the principal advantage of scaling functions is their simplicity. At the same time, their main drawback is the impossibility of deriving quantitative characteristics.

3.3 Analysis of the distribution of atomic chain lengths with the kinetic Monte Carlo method

We now discuss another approach to the analysis of the length distribution of atomic chains with the example of Co/Cu(775) and Ag/Pt(997) systems. In this approach, the KMCM is used; this is laborious, because the density functional theory must be used to evaluate energy characteristics such as diffusion barriers and binding energies [37–39, 83]. Employing a very simple theoretical model in combination with the KMCM allows fixing these parameters variationally [84].

The length distributions of Co/Cu(775) atomic chains obtained with the KMCM for two different temperatures, 160 and 190 K, are shown in Fig. 12a. As the temperature increases, the mean length of cobalt chains and its mean square deviation increase. For Co/Cu(775), the distribution

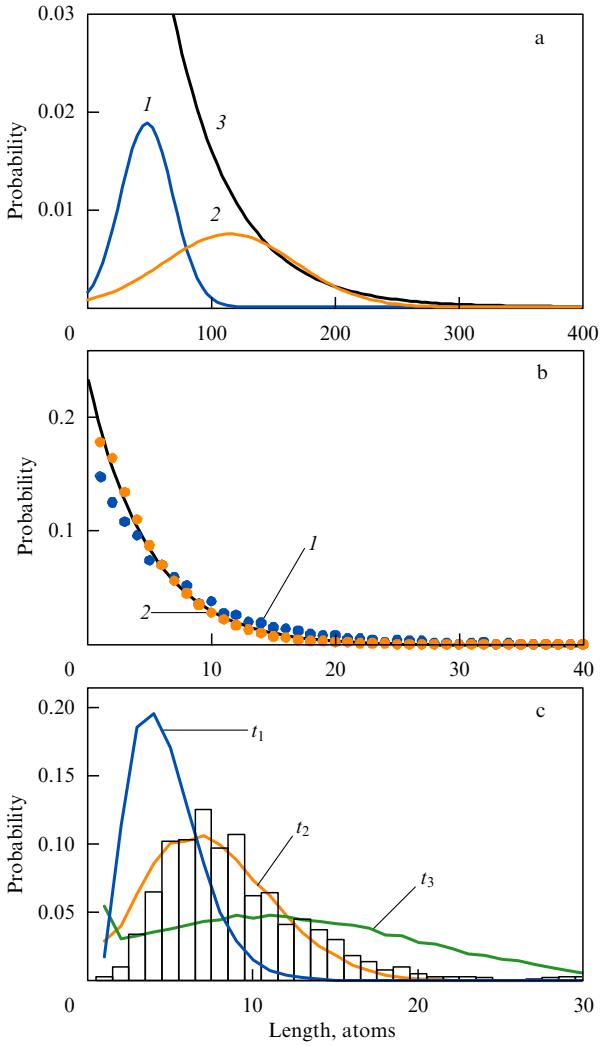

Figure 12. (Color online.) Length distributions of (a) Co/Cu(775) and (b) Ag/Pt(997) atomic chains for temperatures of 160 K (*1*) and 190 K (*2*). The solid black line shows the result of fitting in the framework of the one-dimensional lattice gas model [32]. (c) Length distributions for chains Ag/Pt(997) at $T = 100$ K depending on the duration of the experiment ($t_1 = 1$ h, $t_2 = 5$ h, and $t_3 = 1$ day). The histogram is taken from experimental study [31].

of chain lengths is of the second distribution type, having one maximum, is well approximated by the normal distribution, and is poorly approximated by the equilibrium distribution (curve *3* in Fig. 12a). But a different situation is observed for Ag/Pt(997). As the temperature increases, the distribution of chain lengths changes little and is approximated well by the equilibrium distribution (Fig. 12b).

The cause of this difference is an order-of-magnitude difference between the Co/Cu(775) and Ag/Pt(997) binding energies, which means that diffusion processes occur at different rates in these two systems. For example, for atomic chains of silver, the binding energy is $E_{\text{bind}} = 0.06$ eV, and at 160 K the system reaches thermodynamic equilibrium in a few seconds. If the temperature is decreased, the time to reach thermodynamic equilibrium increases considerably. As can be seen from Fig. 12c, at 100 K the Ag/Pt(997) system does not even reach thermodynamic equilibrium in several days. Concurrently, however, a maximum for single atoms (curve t_3 in Fig. 12c) starts transpiring. We note that, at temperatures below 105 K, atoms of silver have reduced mobility near the

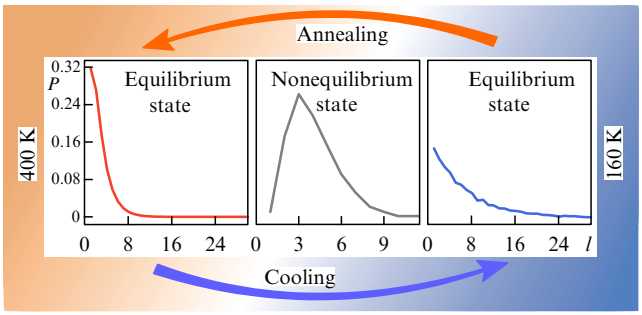

Figure 13. Diagram showing how the length distribution of atomic chains changes in the course of cooling or annealing [39].

step, and therefore at low temperatures the atomic chains do not arrive at equilibrium within the time of the experiment.

In most cases, one-dimensional atomic structures are obtained by annealing at a temperature above room temperature, and the system reaches equilibrium rather soon. Prior to making measurements, the sample is cooled. We consider the transition from one equilibrium state to another under cooling in more detail. At the initial instant at a high temperature, the atomic chains are in equilibrium (Fig. 13, left). In equilibrium, the number of atoms detached from the chain is equal to the number of atoms attached to it. As the temperature decreases, the speed of single atoms decreases, and the lifetime of the chains increases. Because the mean lifetime of short chains is much less than that of long ones, they rapidly decay. Thus, the number of short chains decreases, and the number of long chains increases. At that instant, atomic chains are in a nonequilibrium state (Fig. 13, center). Simultaneously, the distance between chains increases. When it becomes critical, an atom detached from one chain fails to attach to another chain in the available time. In this case, the number of single atoms increases, as does the number of short chains located between two long chains. Consequently, a second, single-atom, maximum appears in the distribution of chain lengths. The system next arrives at equilibrium and is then described well by the model of a one-dimensional lattice gas (Fig. 13, right). Thus, under cooling or annealing, one-dimensional structures pass from one equilibrium state to another via a nonequilibrium state, which is indeed observed experimentally. We see from Fig. 12c that the results of modeling are in good agreement with experimental data.

Studies of the evolution of one-dimensional atomic structures by the KMCM show that the distribution of lengths of one-dimensional structures depends not only on external parameters of the experiment but also on time. At low temperatures, the lifetime of many one-dimensional structures is much longer than the experiment duration time, and they are therefore in a nonequilibrium state. It hence follows that experimental data cannot be analyzed using models in which one-dimensional structures are regarded as equilibrium.

The above examples qualitatively show how the size of one-dimensional structures depends on various external parameters. Yet, a problem in fundamental physics is to find the values of physical quantities from the size distribution of one-dimensional structures. Currently, the only way to find the binding energy and other energy characteristics is still to compare experimental data with modeling results. Other approaches are either inapplicable or give only a qualitative estimate.

4. Structural properties of atomic wires

The physical properties of metallic atomic chains and wires largely depend on their size, shape, and chemical composition. It is therefore important and relevant to study structural properties and to determine stability conditions of one-dimensional structures.

4.1 Determining the structure and chemical composition of atomic chains

Recently, scanning tunneling microscopy has been enjoying wide use in studying atomic one-dimensional structures. The method has a high resolving power, which allows obtaining information on the geometry and structure of such systems. However, an STM does not allow the chemical composition of atomic structures to be determined. When chains form on the surface (see Fig. 2 or Fig. 14), an STM alone is sufficient for determining their structure. But when atomic chains immersed into the surface are investigated, the use of an STM to extract their structural properties is insufficient. This is why combinations of diverse methods are used to study structural properties: either several experimental methods or experimental methods together with computer modeling.

In Fig. 14a, b, we show an example of STM images of atomic chains $Co_{0.5}Ni_{0.5}O_2$ (a) and $Co_{0.67}Ni_{0.33}O_2$ (b). The oxygen atoms cannot be seen in the STM image, but, knowing the relations between atoms in the alloy, we can determine the chemical composition of atomic chains. For example, in Fig. 14a, exactly half the dots are bright and the other half are dim, but the number of bright dots in Fig. 14b is 50% of the number of dim dots. By analyzing these two STM images, we can conclude that the bright dots are the Ni atoms, and the dim dots are the Co atoms. Knowing the chemical composition of atomic chains, we can then study their properties. As can be seen from Fig. 14c, Co atoms in the chain are closer to the surface than the Ni atoms, and therefore interact more strongly with the surface atoms. We note that, besides Co and Ni shown in Fig. 14a, b, atomic chains up to 500 atoms in length also form from oxides of alloys of other transition metals. Such chains of different transition metal alloys offer a unique possibility of designing complicated systems, for example, magnetic structures for memory elements, in which ferromagnetic chains would be separated by antiferromagnetic or nonmagnetic chains [12].

This shows that the use of an STM does not allow determining the chemical composition of a nanostructure. This is especially transparent for materials with atoms of several types, because it is unclear which atom type is observed in which position. Moreover, STM images do not pertain directly to specific atoms but map the electron density distribution. For semiconductors, the electron density maximum corresponds to atomic bonds, and for metals, to atoms. Therefore, in order to determine the structure, an STM is used together with calculations in the framework of the density functional theory [19, 24, 69, 120–125]. This method allows determining the chemical composition of nanostructures, but has various limitations: the number of atoms in the computation cell, the modeling time, etc. In addition, computations require specifying the initial configuration that would be sufficiently close to the real structure.

As an example of such a multifaceted application of an STM and theoretical calculations, we consider the Pt/Ge(001) system. As can be seen from Fig. 1c, one-dimensional structures form on the Ge(001) surface under sputtering

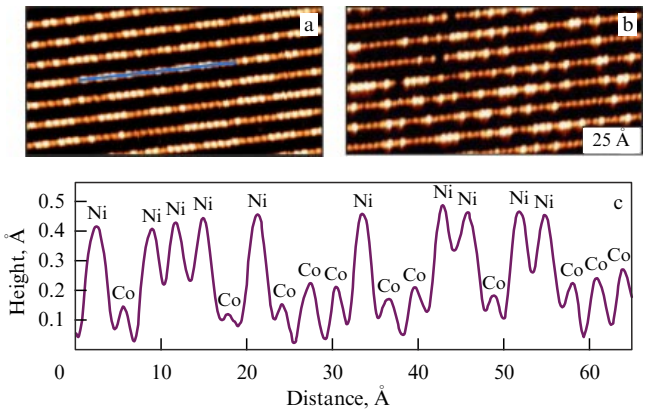

Figure 14. STM images of atomic chains (a) $Co_{0.5}Ni_{0.5}O_2$ and (b) $Co_{0.67}Ni_{0.33}O_2$. (c) Displacement of $Co_{0.5}Ni_{0.5}O_2$ chain atoms relative to the surface [12].

with Pt atoms. Despite the existence of excellent-quality STM images where the positions of individual atoms and dimers can be seen, the real atomic structure of wires remains undetermined, because the STM does not allow finding the chemical composition. The following approach was used to determine the composition and structure of atomic Pt wires on the Ge(001) surface [18, 21, 24, 120, 123, 126]. First, a model of the surface with atomic wires was constructed, as is shown in Fig. 15a. Next, STM images for filled (Fig. 15b, left) and unfilled (Fig. 15b, right) states were simulated. As can be seen from Fig. 15, the simulated STM image agrees with the experimental one. In the case where the simulated STM image does not agree with the experimental one, a new model is proposed and the algorithm is repeated.

Several models of the structure of atomic wires were proposed in the papers cited above. For example, in the model in [126], the Pt atoms are located between two rows of surface Ge dimers. The analysis of the electron density reveals a significant degree of hybridization of the Pt atom orbitals. This is why the STM reveals the wires made up of dimers. In another study [123], a structure model was proposed in which the Pt atoms are immersed into the surface layer, and above them the Ge dimers form one-dimensional structures. A similar model was developed in [19, 24]. There, the immersed wires made of Pt atoms interlace with rows of surface dimers located nearby. Every second surface dimer then decays.

However, comparing an image obtained experimentally and with the help of modeling can be insufficient for determining the geometry and chemical composition. This is why other characteristics are sometimes compared in order to find the nanostructure parameters, for example, the conductance spectrum with the density of states of one-dimensional structures [18, 19]. A comparison of the differential conductance spectrum with the computed averaged density of states at different temperatures is shown in Fig. 15c. At a low temperature, the density of states at the Fermi level ($E = 0$) is equal to zero. The energy gap also occurs at an energy of 0.25 eV below the Fermi level in the direction of the atomic wire, which agrees with experiment [127]. The peak of the density of states between two energy gaps is determined by the d states of Pt atoms and sp^3 states of Ge atoms. As the temperature increases, the localized state is washed out, and the energy gaps on the Fermi level vanish at the energy of

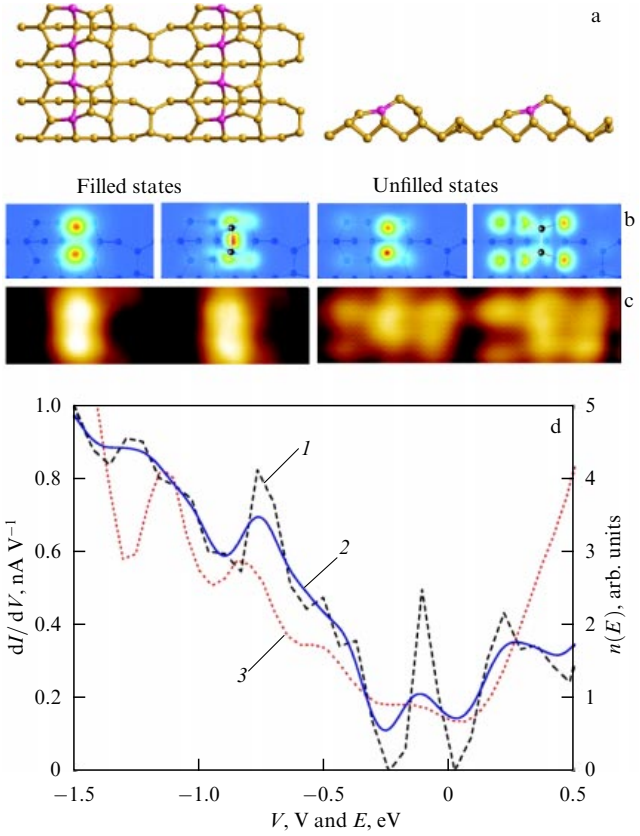

Figure 15. (a) Model of Pt atomic wires on a Ge(001) surface. Top view (left) and side view (right). Comparison of (b) simulated and (c) experimental STM images for filled and unfilled states [19]. (d) The calculated density of states for Pt/Ge(001) at different values of $k_B T$: 10 meV (*1*), 100 meV (*2*), and the differential conductance spectrum dI/dV (*3*).

0.25 eV (Fig. 15d). Thus, at low temperatures, one-dimensional atomic wires of Pt on the Ge(001) surface are semiconductors [127], whereas at room temperature they are metals [19].

4.2 Structural phase transition in atomic chains of cobalt on the vicinal surface of copper

In some cases, a surface carrying one-dimensional structures has several phases [17, 18, 61]. We consider this phenomenon in detail with the example of atomic chains of cobalt on the vicinal surface of copper. In [61], the existence of two phases in long atomic chains of cobalt was found experimentally. On the Cu(775) surface at $T = 5$ K, the atoms are located at different distances from each other in these phases (Fig. 16). STM measurements have shown that, at low temperatures, the distances between a cobalt atom and two of its nearest neighbors are 0.20 and 0.31 nm, which means that the dimerization process is observed. For comparison, the interatomic distance for triangular atomic islets of cobalt on the surface of copper is 0.250–0.256 nm. As the temperature changes from 5 to 91 K, the shortest distance between atoms in the chain changes from 0.200 to 0.256 nm. Hence, two different phases of the chains are observed at temperatures below 91 K. As the chain length increases, the effect of edge atoms diminishes, and as a result dimerization is observed. Therefore, the structure of short atomic chains of cobalt located near a step on the vicinal surface of copper (111) is different from that of long atomic chains of cobalt [128]. This

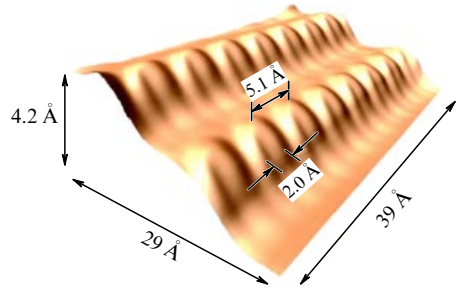

Figure 16. STM image of a dimerized cobalt chain on the vicinal surface of copper [61].

is because the cobalt atoms at the edges of the chain are freer, and, hence, the interaction between the cobalt atoms and copper atom of the step can vary considerably. For example, the chain of five Co atoms on the Cu(554) surface has a complicated shape resembling the letter M. The edge atoms, together with the central atom, are displaced downward, while the other atoms are displaced upward. The surface copper atoms under the atomic chain are then displaced downward.

Dimerization of atomic chains of cobalt was also confirmed using calculations in the framework of the density functional theory [62, 129], although it had been asserted previously that the density functional theory [130] does not allow finding a dimerized structure of atomic chains of cobalt on stepped copper surfaces [131]. This controversy occurred because magnetic interaction in nanostructures is highly sensitive to the interatomic distance [27, 128, 132–134]. Determining the equilibrium state therefore requires numerous calculations with different initial positions of atoms in the system and with different computation cells, which was not done in the earlier study [131]. For example, the vicinal surface of copper was modeled as periodically repeated layers comprising 8 atomic layers in [131] and 60 atomic layers in [62].

The energy diagram of atomic chains of cobalt near an atomic step of the surface of copper is shown in Fig. 17. The following configurations were selected: a chain with an antiferromagnetic ordering of spin and a uniform arrangement of atoms (Fig. 17a), a dimerized chain with ferromagnetic ordering of spins (Fig. 17b), a nondimerized chain with ferromagnetic ordering of spins (Fig. 17c), and a chain with zero spins and a uniform arrangement of atoms (Fig. 17d). It follows from the energy diagram (Fig. 17e) that the most energetically advantageous state is B, but the difference in energy with respect to state C (dimerization energy ΔE) is very small. It is equal to 2 meV per atom for the Cu(111) surface and $\Delta E = 4$ meV per atom for the Cu(332) surface, which explains the instability of dimerized chains upon increasing the temperature above some critical value. However, the dimerization energy of the cobalt chain is much higher on the copper (775) surface (6 meV per atom) than on the copper (111) surface (2 meV per atom) [62, 129]. Interatomic distances in the dimers for the respective (775) and (111) copper surfaces are 0.23 and 0.24 nm. In all these cases, the stepped surface consists of small terraces, and atomic chains of Co located near neighboring steps interact with each other. Thus, the dimerization energy of the chains also depends on the width of the surface terraces.

Formation of the dimerized phase in atomic chains of cobalt is strongly affected by the electric field. It has been

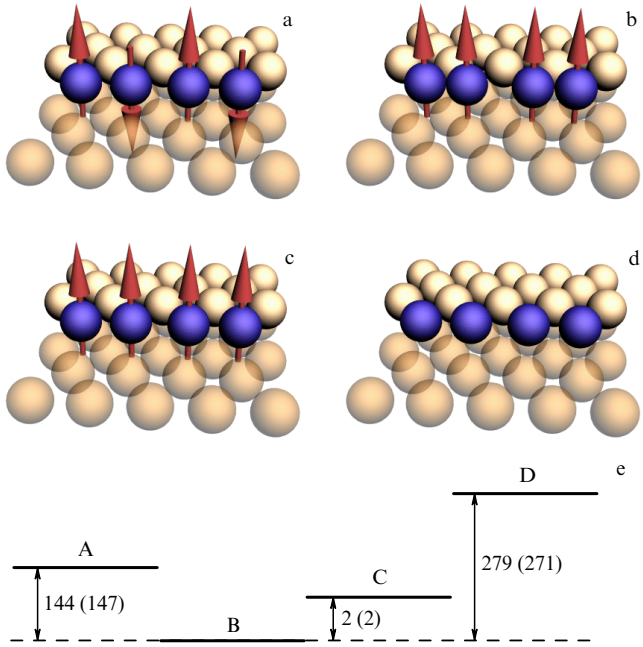

Figure 17. (a) Antiferromagnetic, (b) dimerized ferromagnetic, (c) non-dimerized ferromagnetic, and (d) zero-spin configurations of Co chains on a vicinal Cu(111) surface; (e) energy diagram with specific binding energy values for atoms in the chain (meV per atom) for a B-type step. Values for A-type steps are shown in parentheses [62, 129].

established experimentally that, the greater the potential difference between the STM tip and the surface, the higher the temperature at which dimerization of the atomic chain is observed. This is because the surface and the atomic chain deform under the action of the electric field [135]. It is known that the STM tip is not smooth. Therefore, on the surface of the main tip, there is a mini-tip (one or several atoms), which is just what is used for nanostructure scanning [136]. If the distance between the tip and an atomic chain is sufficiently small, then the chain is significantly deformed under the action of the electric field near the STM tip. When the tip is scanning along the atomic chain, the deformed domain changes continuously, making it impossible to determine the distances between atoms with high accuracy, because the STM images are blurred. As the distance between the chain and the STM tip increases, the effect of the mini-tip becomes inessential, and in that case the domain of deformation has a size of several nanometers [135]. The curvature radius of the STM tip is 2 to 30 nm, which is comparable to the mean length of the relevant chains. The STM tip then alters the properties of the entire chain when interacting with it. If we eliminate the effect of the mini-tip, then the dimerization phenomenon for atomic chains of cobalt depends only on the potential difference between the tip and the chain [135]. This is confirmed by results of calculations showing that the chain dimerization energy ΔE in the interaction with the STM tip changes from 2 to 18 meV per atom [62, 129]. Therefore, the greater the potential difference between the STM tip and the surface, the greater the temperature interval within which atomic chain dimerization occurs [61].

Modeling the phase transition in atomic chains of Co on the Cu(775) surface has shown that the phase transition temperature also depends on the length of the atomic chains

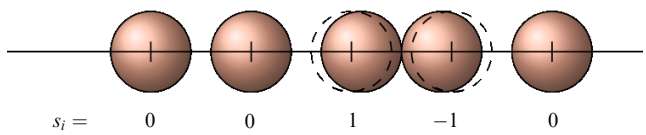

Figure 18. Calculation of the order parameter η.

[62, 129]. For this purpose, the Metropolis algorithm [137] was used in the framework of a simple model where the state of an atomic Co chain is characterized by the order parameter

$$\eta = \frac{2}{N}\left|\sum_{i=1}^{N/2} s_{2i}\right|, \tag{38}$$

where N is the number of atoms in the chain and s_i is the parameter determining the position of the ith atom with respect to its ideal position. We have $s_i = 0$ for an atom in the ideal position, $s_i = -1$ for an atom displaced to the left, and $s_i = 1$ for an atom displaced to the right (Fig. 18). The summation in expression (38) ranges all even sites, and therefore in the case of a totally dimerized chain, $\eta = 1$. An atom with a number i and its displacement direction $\Delta s = \pm 1$ are chosen at random at each step.

The system evolution is governed by the following rules. If $s_i = 0$ and $s_{i+\Delta s} = 0$, then the system passes into a new state $s_i = \Delta s$ and $s_{i+\Delta s} = -\Delta s$, which means the formation of a dimer from the ith and $(i + \Delta s)$th atoms, leading to a decrease in the total energy of the system by $2\Delta E$, which is the per atom energy difference between the dimerized chain and the chain with equal interatomic distances (the dimerization energy). Otherwise, if $s_i = \pm 1$ and $\Delta s = -s_i$, then the system passes into a new configuration $s_i = 0$ and $s_{i+\Delta s} = 0$ with the probability $\exp(-2\Delta E/k_{\mathrm{B}}T)$. The decay of a dimer is attended by an increase in the total energy by $2\Delta E$.

In Fig. 19a, we show the temperature dependence of the order parameter η for a chain consisting of 32 Co atoms. At zero temperature, all atoms in the chain make up dimers, and hence $\eta = 1$. As the temperature increases, the symmetry of the chain is violated, and the order parameter η monotonically decreases and tends to zero. This situation is typical of a second-order phase transition. The phase transition temperature T_{C} is determined by the decrease in the maximum of the order parameter derivative taken with the minus sign, $-\mathrm{d}\eta/\mathrm{d}T$ (Fig. 19b). For example, for a chain 32 atoms in length with a dimerization energy of 16 meV, the phase transition temperature is 71 K, which agrees with experiment [131].

We note the dependence of the phase transition temperature on the chain length (the size effect). As the length of the chain increases, the phase transition temperature decreases and tends to zero in the limit of an infinite chain (Fig. 19c), which is in agreement with the one-dimensional Ising model [138]. The dependence of the phase transition temperature on the length of the chain is approximated well by the formula

$$T_{\mathrm{C}} = A\,\frac{\Delta E}{\ln N}, \tag{39}$$

where $A = 20.16$ K meV^{-1}. Thus, the phase transition temperature in one-dimensional structures depends not only on the potential difference between the STM tip and the sample and on the width of terraces on the underlying surface, but also on their length.

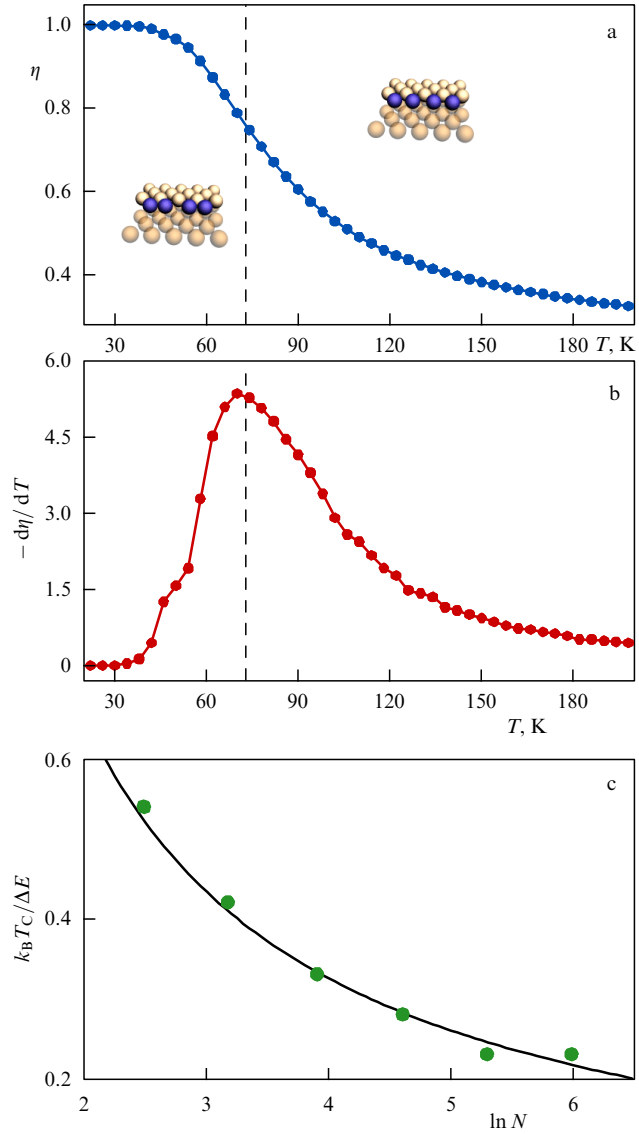

Figure 19. Dependence of (a) the order parameter η and (b) its derivative $-\mathrm{d}\eta/\mathrm{d}T$ on temperature. The length of the Co chain is 32 atoms, $\Delta E = 16$ meV. The order parameter η was determined from the results of 2000 numerical experiments [62]. (c) Dependence of the phase transition temperature T_C on the length of the chain. The line shows the approximation in (39).

5. Quantum effects in atomic chains

Vigorous development of electronics and computation methods requires constant miniaturization of various devices, first and foremost, of data storage elements. One of the ways to achieve such a minimization and to increase the density of recording information is to use information storage elements in the form of magnetic atomic wires placed on various surfaces. This requires knowing not only how atomic wires can be formed but also what their electronic properties are.

5.1 Density of states of a two-dimensional electron gas

To analyze the electronic properties of atomic chains and the effect exerted on them by surface states, we first consider the density of states of an idealized surface. A simple model is provided here by a two-dimensional electron gas. In the framework of this model, we can obtain an expression for the density of states of the idealized surface.

We consider the model of a two-dimensional electron gas in detail and obtain an expression for its density of states. We assume that the electrons can move freely only in the xy plane. In the transverse direction (z axis), the energy is quantized and takes discrete values E_{n_z}, where n_z is a quantum number. The total spectrum is then also discrete–continuous, but with only two continuous degrees of freedom:

$$E = E_{n_z} + \frac{\hbar^2(k_x^2 + k_y^2)}{2m} = E_{n_z} + \frac{\hbar^2 k^2}{2m} . \tag{40}$$

For one subband, the number of allowed states in an annulus with an area of $2\pi k\,\mathrm{d}k$ (where k is the wave number) is equal to the number of cells $(2\pi/L)^2$, where L is a characteristic size. Therefore, the number of quantum states is equal to

$$\mathrm{d}N = 2\frac{L^2}{(2\pi)^2} 2\pi k\,\mathrm{d}k , \tag{41}$$

where the factor 2 accounts for two allowed values of the spin quantum number for each allowed value of $\mathbf{k}$. We now rewrite Eqn (41) in terms of energy:

$$\mathrm{d}N = \frac{L^2 m}{\pi\hbar^2}\,\mathrm{d}E . \tag{42}$$

For the density of states per unit area for a subband, we can use (42) to obtain

$$\rho^{2\mathrm{D}}(E) = \frac{m}{\pi\hbar^2} . \tag{43}$$

For a two-dimensional system, as noted above, there is a constraint along one direction (z), and therefore expression (43) must be summed over all quantum numbers n_z:

$$\rho^{2\mathrm{D}}(E) = \frac{m}{\pi\hbar^2}\sum_{n_z} \Theta\left(E - E_{n_z}\right) , \tag{44}$$

where $\Theta(E - E_{n_z})$ is the Heaviside function.

The density of states of the two-dimensional electron gas is zero for energies below the first energy level. For an energy equal to the first level (the bottom of surface states), the density of states increases jumpwise and then remains constant until the next energy level; such a jumpwise increase occurs at each level. In Fig. 20a, for states of the two-dimensional electron gas, we show the experimental conductance spectrum that forms near the surface. Both in the model of the two-dimensional electron gas and in reality, the density of surface states has the shape of a step (Fig. 20a). For example, the bottom of surface states for the Ag(111) surface is 67 meV, and for Cu(111), 445 meV below the Fermi level [139]. For vicinal surfaces, surface states are displaced toward higher energies compared with the Cu(111) surface [140–142]. Their position depends on the width of the terrace. In particular, for Cu(443) and Cu(554), the positions of the bottom of surface states calculated in the framework of density functional theory are −170 and −300 meV (with respect to the Fermi level), and the corresponding experimental values are −150 and −250 meV [140–142]. In addition, decorating a vicinal surface with magnetic atomic wires also has a significant effect on surface states [142, 143].

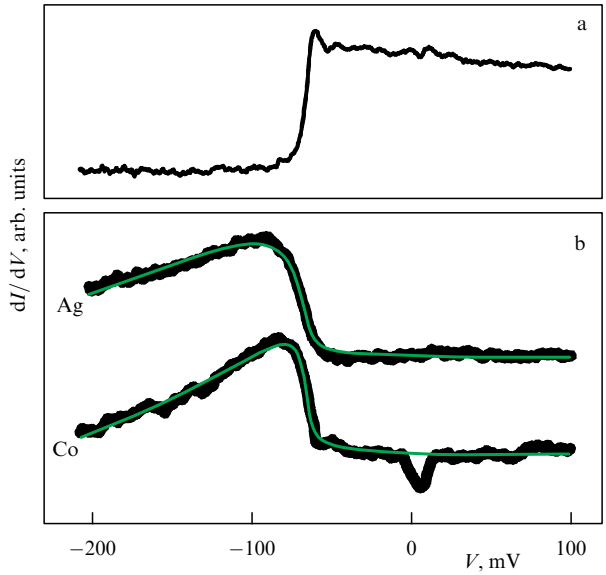

Figure 20. Experimental conductance spectrum dI/dV of (a) a clean Ag(111) surface and (b) Ag and Co atoms on an Ag(111) surface [139].

5.2 Localization of surface states in single atoms and the edge state of atomic chains on a surface

If an atom or atomic chain is placed on a surface, the density of states differs significantly from the density of states of a clean surface. For example, near the edge of a chain or an atom, the density of states already has the shape of a peak, located near the bottom of the surface states. Such edge states for atomic chains and atoms were first revealed experimentally in [28, 139, 144]. The conductance spectra measured near Ag and Co atoms located on the Ag(111) surface are shown in Fig. 20b. The conductance spectra of atoms have peaks at energies of −70 meV for Ag(111) and −450 meV below the Fermi level for Cu(111), which corresponds to the bottom of the surface states shown in Fig. 20a.

For a realistic description of the localization of a surface state on single or edge atoms, we must recall the coupling between surface and bulk states [139, 145]. For this, we consider an extended Newns–Anderson model [146, 147], which in our case describes an atom in a state $|a\rangle$ with energy ε_a, interacting with the bulk Bloch states $|q\rangle$ and with surface states $|k\rangle$ of the Cu(111) substrate. The Hamiltonian of the system can be represented in the form

$$\mathcal{H} = \begin{pmatrix} \varepsilon_a & V_{a\mathbf{q}} & \tilde{V}_{a\mathbf{k}} \\ \tilde{V}^*_{a\mathbf{q}} & \varepsilon_{\mathbf{q}} & 0 \\ \tilde{V}^*_{a\mathbf{k}} & 0 & \tilde{\varepsilon}_{\mathbf{k}} \end{pmatrix}, \tag{45}$$

where $\varepsilon_{\mathbf{q}}$ is the energy of bulk electrons, $\tilde{\varepsilon}_{\mathbf{k}}$ is the energy of surface electrons, and $V_{a\mathbf{q}}$ and $\tilde{V}_{a\mathbf{k}}$ are matrix elements of the interaction. Here, $\mathbf{k}$ denotes a two-dimensional Bloch wave vector and $\mathbf{q}$ is a three-dimensional vector.

The conductance spectrum registered when the STM tip is located over an atom can be considered the density of states of the atom $n_a(E)$. Using the formalism of the Green's functions [139], we obtain

$$n_a(E) = \frac{1}{\pi} \frac{\Delta(E)}{\left[E - \varepsilon_a - \Lambda(E)\right]^2 + \Delta(E)^2}. \tag{46}$$

In the imaginary part of the eigenenergy $\Sigma(E) = \Lambda(E) + i\Delta(E)$, the coupling of the atomic level to both bulk states $\Delta_b(E)$ and surface states $\Delta_s(E)$ is taken into account:

$$\Delta(E) = \Delta_b(E) + \Delta_s(E). \tag{47}$$

The bulk contribution

$$\Delta_b(E) = \pi \sum_{\mathbf{q}} |V_{a\mathbf{q}}|^2 \delta(E - \varepsilon_{\mathbf{q}}) = \Delta_b \tag{48}$$

is assumed to be constant in the entire energy range of interest. The contribution of surface states

$$\Delta_s(E) = \pi \sum_{\mathbf{k}} |\tilde{V}_{a\mathbf{k}}|^2 \delta(E - \tilde{\varepsilon}_{\mathbf{k}}) = \Delta_s \Theta(E - E_0) \tag{49}$$

is determined by a stepped function of the density of surface states. The real part $\Lambda(E)$ of the eigenenergy $\Sigma(E)$ can be found if we know $\Delta(E)$, using the Hilbert transformation [139]. The density of surface states has a logarithmically divergent term at the energy equal to E_0 [148],

$$\Lambda(E) = \frac{\Delta_s}{\pi} \ln|E - E_0| + C, \tag{50}$$

where C is a constant.

To quantitatively estimate the experimental results, we must find the density of surface states in the framework of the model as precisely as possible [139, 149]. For this, we must take the lifetime of electrons in a surface state into account, which then leads to smoothing the density of states and a quantitative coincidence with the experimental conductance spectrum. In this case, the density of states can be represented as [149]

$$n(E) = \frac{1}{2} + \frac{\arctan\left[2(E - E_0)/\Gamma\right]}{\pi}, \tag{51}$$

where Γ is the inverse lifetime of the surface state. The real part of the eigenenergy then takes the form

$$\Lambda(E) = \frac{\Delta_s}{2\pi} \ln\left[(E - E_0)^2 + \left(\frac{\Gamma}{2}\right)^2\right] + C. \tag{52}$$

The constant can be eliminated if we renormalize the energy of the impurity atom level. The results of a theoretical calculation of the density of states of Ag and Co atoms on an Ag(111) surface are shown in Fig. 20b (bright line). In constructing the density of states of an atom, the Newns–Anderson model parameters were fixed by fitting to the experimental data [139].

Such localized surface states appear not only in conductance spectra of single atoms on the surface but also for edge atoms of the chain. In Fig. 21b, we present the conductance spectrum of a chain made of seven Au atoms on an Si(553) surface whose STM image is shown in Fig. 21a. Measurements were made with different positions of the STM tip, which are denoted by numbered dots in Fig. 21a. As can be seen from Fig. 21b, for an edge atom, the conductance spectrum has a characteristic peak, which disappears at a distance from the chain. For the next-to-last atom in the chain, the peak in the conductance spectrum splits into two. This phenomenon is explained in the next section. We note that localized surface states disappear at a distance of 1 nm

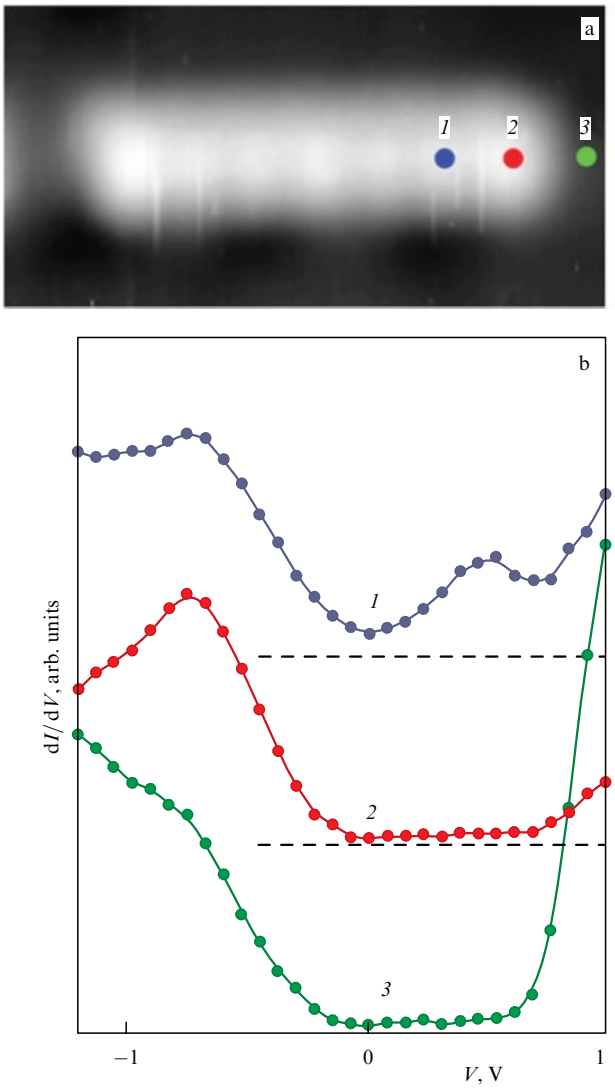

Figure 21. (a) STM image of an atomic chain of seven gold atoms on an Si(553) surface. (b) Experimental conductance spectrum dI/dV measured at different points near the edge of the atomic chain. Curve *1* corresponds to the conductance spectrum of the next-to-last atom in the chain, and curve *2* to the edge atom; curve *3* shows the conductance spectrum of the surface near the atomic chain [28].

from the atom [28, 150]. In addition, the results of calculations in the density functional theory framework show that, in the case of magnetic impurities, localized surface states are spin-polarized [150–152]. The position of characteristic peaks can then differ slightly in energy for electrons with different spin orientations.

5.3 Density of states of atomic chains

We next discuss the density of electron states in atomic chains. Changes in the structure and size of atomic chains lead to changes in their electronic properties. The size of atomic chains is determined by the number of atoms in them and the interatomic distance. The density of states of atomic chains is measured with scanning tunneling spectroscopy. For this, the STM tip is positioned at a point where the electronic properties of the system are to be investigated, and the conductance spectrum is measured. The conductance spectra measured in the middle of gold atom chains of various lengths on an NiAl(110) surface are shown in Fig. 22. As can be seen

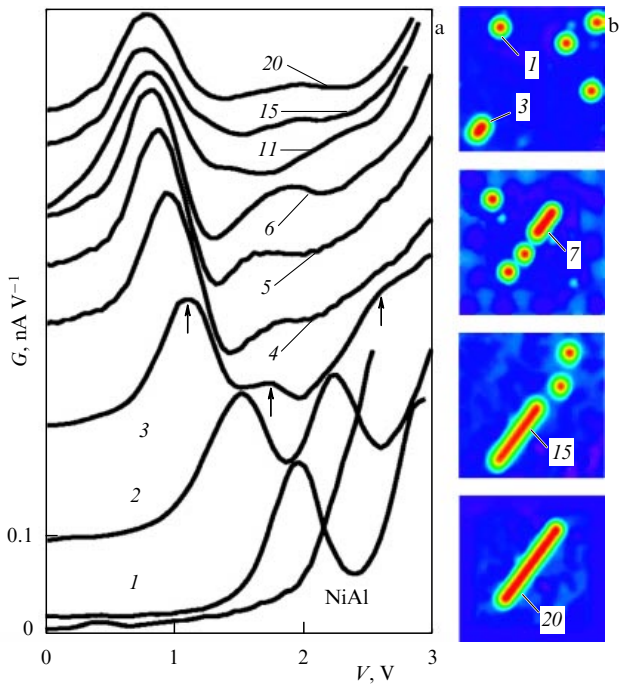

Figure 22. (a) Conductance spectra measured in the middle of Au atom chains of different lengths (numbers on the curves indicate the number of atoms in each chain). (b) STM image of atomic Au chains of different lengths on an NiAl(110) [153] surface (numbers indicate the number of atoms in each chain).

from Fig. 22, the density of states of atoms in the middle of the chain increases sharply and falls off smoothly.

An analytic expression for the density of states of chains can be derived in the framework of the one-dimensional electron gas model. An argument similar to the one presented in the foregoing allows obtaining an expression for the density of states of the one-dimensional system as [27]

$$\rho^{1D}(E) = \frac{\sqrt{2m}}{\pi\hbar} \sum_{n_y, n_z} \frac{\Theta(E - E_{n_y, n_z})}{\sqrt{E - E_{n_y, n_z}}}\,, \tag{53}$$

where n_y and n_z are quantum numbers.

The density of states in the idealized one-dimensional case, in accordance with expression (53), must increase discretely and then fall off as $1/\sqrt{E}$ to the next energy level. Such a jumpwise increase and further decrease in the density of states occurs at each level. Thus, the density of states of a one-dimensional system consists of peaks corresponding to each energy level. However, in contrast to the idealized case, peaks of the density of states of atoms are somewhat smeared in energy in a chain, because it has a finite length and its atoms interact with the surface.

The conductance spectrum of a single atom of gold on an NiAl(110) surface has a resonance shaped like the normal distribution. The conductance spectrum resonance occurs at a voltage of 1.95 V (see Fig. 22). When a second gold atom is added in an adjacent position, a dimer forms, entailing a change in the electronic properties of the gold atoms. The conductance spectrum resonance of a single atom at the voltage of 1.95 V is split into a doublet, with peaks at 1.50 and 2.25 V, which is indicative of a strong binding between the atoms in the dimer. The energy splitting is similar to the well-known example of two 1s

states of hydrogen making bonding and antibonding levels in the hydrogen molecule. The formation of a chain of three gold atoms shifts one peak to 1.10 V and the other to 2.60 V. A third peak also appears in the conductance spectrum at 1.80 V due to the overlap of electron orbitals of the gold atoms. All the peaks are marked with arrows in Fig. 22.

With further changes in the length of a chain, changes in the conductance spectrum or the density of states are observed for atoms in the middle of the chain [153]. We can see from Fig. 22 that the conductance spectrum peaks shift toward lower energies. Thus, unfilled electron states are displaced toward the Fermi level. The displacement of peaks in the density of states is proportional to L^{-2}, where L is the length of the atomic chain.

The observed changes in the conductance spectrum of atomic chains show a dependence of the electronic properties of the system on its geometry. For example, a correlation is observed between quantum effects and structure properties at the atomic scale. Knowing the dependence of the electronic properties of one-dimensional structures on their length, it would be possible to control the properties of the structures and thus to design electronic devices. In addition, edge states can also be useful for designing electronic devices, because they allow determining the edge of one-dimensional structures using conductance spectrum measurements.

5.4 Rashba effect

In [154], Rashba demonstrated that, if a crystal has one axis of high symmetry (of at least the third order) and an invariant vector $\mathbf{n}$ is oriented along it, then the Hamiltonian of spin–orbit coupling of the electron has the form

$$\hat{H}_{\mathrm{R}} = \alpha \mathbf{n}\,[\boldsymbol{\sigma} \times \hat{\mathbf{k}}]\,, \tag{54}$$

where $\boldsymbol{\sigma}$ are the Pauli matrices, $\hat{\mathbf{k}} = -\mathrm{i}\nabla$ is the wave vector operator of the electron, and $\alpha = \mathrm{const}$. Hamiltonian (54) lifts the two-fold spin degeneracy of the energy spectrum in a zero external magnetic field ($\mathbf{B} = 0$) and leads to a number of nontrivial effects at $\mathbf{B} \neq 0$. Subsequently, the Rashba effect was studied in the case of two-dimensional systems [155, 156], where the vector $\mathbf{n}$ is the normal to the surface. The Rashba effect is being actively studied for various three-dimensional and two-dimensional systems. Interest in the Rashba effect was rekindled with the discovery of graphene and other two-dimensional materials.

Recently, the Rashba effect was actively investigated in one-dimensional systems: atomic wires and chains. To consider an infinite wire or a finite-length wire, we must generalize Rashba Hamiltonian (54) to the case of an inhomogeneous wire ($\alpha \neq \mathrm{const}$). This can be done as [158]

$$\hat{H}_{\mathrm{R}} = \gamma \nabla U(\mathbf{r})\,[\boldsymbol{\sigma} \times \hat{\mathbf{k}}]\,, \tag{55}$$

where $U(\mathbf{r})$ is the potential energy of the electron and $\gamma = \mathrm{const}$. For $\gamma U_{\mathrm{R}}(\mathbf{r}) = \alpha(\mathbf{n}\mathbf{r})$ and $\alpha = \mathrm{const}$, generalized Hamiltonian (55) passes into the one in (54). The total potential energy of the electron $U(\mathbf{r})$, besides the $U_{\mathrm{R}}(\mathbf{r})$ contribution, must contain the potential energy of confinement $U_{\mathrm{c}}(\mathbf{r}_\perp)$, which keeps the electron inside the nanowire. Here, $\mathbf{r}_\perp$ is the radius vector in the plane perpendicular to the nanowire. In what follows, we assume the function $U_{\mathrm{c}}(\mathbf{r}_\perp)$ to be sufficiently smooth for $|\nabla U_{\mathrm{c}}|$ in Hamiltonian (55) to be neglected compared with $|\nabla U_{\mathrm{R}}|$.

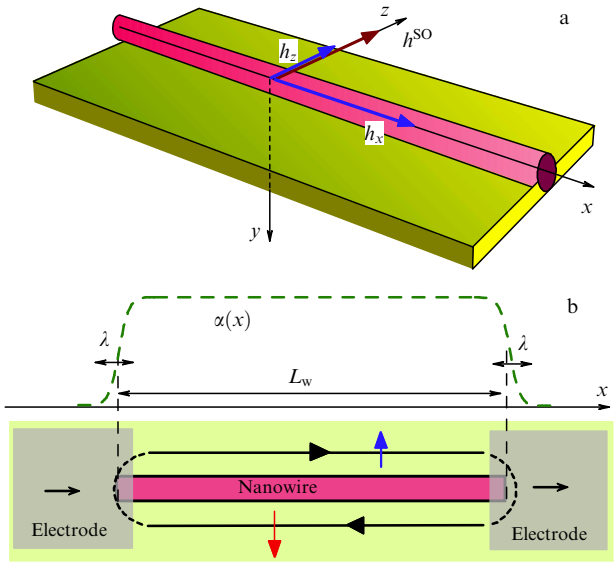

Figure 23. Schematic of (a) an infinitely long nanowire and (b) a finite-length nanowire placed between two electrodes [157]. SO is the spin–orbit coupling.

We first discuss a homogeneous infinitely long wire in the absence of external fields. Following [57], we introduce the coordinate axes as shown in Fig. 23a: x is directed along the nanowire, y is perpendicular to the surface, and z lies in the plane of the surface and is perpendicular to the nanowire. If the direction of the normal to the surface is $\mathbf{n} = (0, -1, 0)$, then the one-electron Hamiltonian is given by

$$\hat{H} = \hat{H}_\perp + \frac{\hat{p}_x^2}{2m^*} + \frac{\alpha}{\hbar}(\sigma_x \hat{p}_z - \sigma_z \hat{p}_x)\,, \tag{56}$$

where

$$\hat{H}_\perp = \frac{\hat{\mathbf{p}}_\perp^2}{2m^*} + U_{\mathrm{c}}(\mathbf{r}_\perp)\,, \tag{57}$$

and m^* is the effective mass of the electron in the nanowire. Knowing the potential energy of confinement $U_{\mathrm{c}}(\mathbf{r}_\perp)$, we can find the eigenfunction $\psi_{\perp,n}(\mathbf{r}_\perp)$ and eigenvalues $E_{\perp,n}$ of Hamiltonian (57). For simplicity, we assume that, at a near-zero temperature of the system ($T = 0$ K), all electrons in the nanowire are at the level with $n = 0$. But if the temperature is different from 0 K, then this approximation implies that we neglected the nanowire thickness, i.e., $U_{\mathrm{c}}(\mathbf{r}_\perp) = -|A|\delta^{(2)}(\mathbf{r}_\perp)$. Averaging Hamiltonian (56) over the wave function $\psi_{\perp,0}(\mathbf{r}_\perp)$ and setting $E_{\perp,0} = 0$, we obtain the one-dimensional Hamiltonian of the electron in the nanowire:

$$\hat{H}_{1\mathrm{D}} = \frac{\hat{p}_x^2}{2m^*} - \frac{\alpha}{\hbar}\,\sigma_z \hat{p}_x\,. \tag{58}$$

Hamiltonian (58), obviously, commutes with the spin projection operator $\hat{s}_z$. The eigenvalues of Hamiltonian (58) are

$$E_{1\mathrm{D}} = \frac{\hbar^2}{2m^*}(k_x - \sigma k_{\mathrm{SO}})^2 - E_{\mathrm{SO}}\,, \tag{59}$$

where $k_{\mathrm{SO}} = \alpha m^*/\hbar^2$, $E_{\mathrm{SO}} = \hbar^2 k_{\mathrm{SO}}^2/2m^*$ (here and hereafter, the index SO refers to spin–orbit coupling), and σ takes the

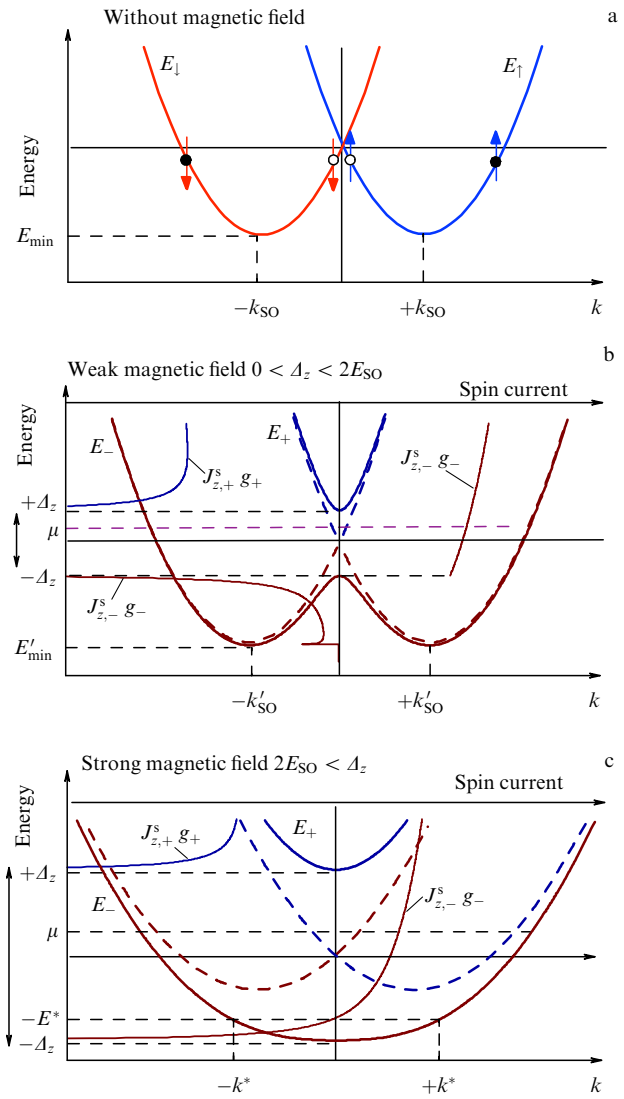

Figure 24. Dispersion law for an electron in an infinitely thin nanowire: (a) in the absence of a magnetic field, (b) in a weak magnetic field, (c) in a strong magnetic field [157].

value +1 for spin-up electrons ($s_z = \hbar/2$) and −1 for spin-down electrons ($s_z = -\hbar/2$). The dispersion law for spin-up and spin-down electrons is given by two parabolas shifted with respect to one another by $2k_{SO}$ (Fig. 24a). In Fig. 25, we represent the dispersion law of electrons in Pt–Si nanowires on an Si(110) surface, in accordance with the data of angle-resolved photoelectron spectroscopy [30]. Near the Γ point, the dispersion law of electrons agrees well with formula (59) for $m^* = -0.66m_e$, $E_{SO} = 81$ meV, and $k_{SO} = 0.12$ Å^{-1}. This implies that $\alpha = 1.36$ eV Å. Because E_{SO} and k_{SO} turned out to be much greater than for the one-dimensional systems investigated previously [159, 160], the authors of [30] called the effect that they revealed in Pt–Si nanowires the gigantic Rashba effect. Subsequently, the gigantic Rashba effect was also observed in a number of one-dimensional systems, such as Pb nanoribbons on an Si(553) surface [161], zigzag Bi chains on an InAs surface [162], and Bi edge clusters on an Si(111) surface [163].

We now consider the wire in an external magnetic field $\mathbf{B} \neq 0$ at zero temperature $T = 0$ K. For this, we must add the term $-(\mathbf{h}\boldsymbol{\sigma})$ to Hamiltonian (58), where $\mathbf{h} = g\mu_B\mathbf{B}/2$, μ_B is Bohr's magneton, and g is the Landé factor. As a result, the

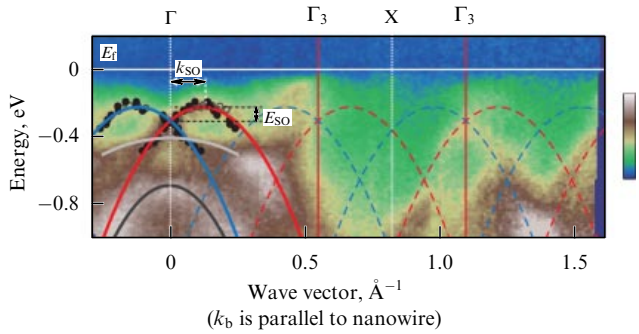

Figure 25. (Color online.) Rashba effect in a Pt–Si nanowire. Data from angle-resolved photoelectron spectroscopy [30].

one-dimensional Hamiltonian of the electron in the nanowire takes the form

$$\hat{H}_{1D} = \frac{\hat{p}_x^2}{2m^*} - \left[\frac{\alpha}{\hbar}\hat{p}_x + h_z\right]\sigma_z - (\mathbf{h}_\perp\boldsymbol{\sigma}_\perp)\,, \tag{60}$$

where $\mathbf{h}_\perp = (h_x, h_y, 0)$ and $\boldsymbol{\sigma}_\perp = (\sigma_x, \sigma_y, 0)$. We see that the nonvanishing component of the magnetic field $h_z \neq 0$ results in the appearance of a piece $-\sigma h_z$ in energy (59), i.e., to shifting one of the parabolas in Fig. 24a upward and the other downward.

Much more interesting results follow in the case of a nonzero magnetic field $\mathbf{h}_\perp \neq 0$. Following [157], we now assume that the magnetic field is directed along the nanowire, i.e., $\mathbf{h}_\perp = (h_x, 0, 0)$. Then, the two branches of the dispersion law of an electron no longer intersect, and a gap $2\Delta_z$ in width appears at $k_x = 0$, with $\Delta_z = |h_x| = |g\mu_B B_x/2|$. Two cases must then be distinguished. For $\Delta_z < 2E_{SO}$, the Rashba effect exceeds the Zeeman effect (Fig. 24b). In that case, the wave number corresponding to the energy minima decreases,

$$k'_{SO} = k_{SO}\sqrt{1 - \frac{\Delta_z^2}{4E_{SO}^2}}\,,$$

and the depth of the minima increases,

$$E'_{min} = -E_{SO}\left(1 + \frac{\Delta_z^2}{4E_{SO}^2}\right).$$

Conversely, for $\Delta_z > 2E_{SO}$, the Zeeman effect exceeds the Rashba effect (Fig. 24b), and the dispersion law for an electron has a single minimum at $k_x = 0$: $E'_{min} = -\Delta_z$.

The most interesting result in [157] is the prediction of a nonvanishing spin polarization $\mathbf{P}$ and spin current $\mathbf{J}^s$ in a nonvanishing magnetic field $\mathbf{h}_\perp = (h_x, 0, 0)$. As was to be expected, the electrons are polarized in the magnetic field direction, i.e., $\mathbf{P} = (P_x, 0, 0)$, where

$$P_x = \frac{1}{\rho}\int\frac{dk_x}{2\pi}\,\frac{h_x\left[f(E_-(k_x)) - f(E_+(k_x))\right]}{\sqrt{(\alpha k_x)^2 + h_x^2}}\,. \tag{61}$$

Here, ρ is the concentration of electrons, $f(E) = \{1 + \exp[(E-\mu)/k_B T]\}^{-1}$ is the Fermi–Dirac distribution, and

$$E_\pm(k_x) = \frac{\hbar^2 k_x^2}{2m^*} \pm \sqrt{(\alpha k_x)^2 + h_x^2}\,.$$

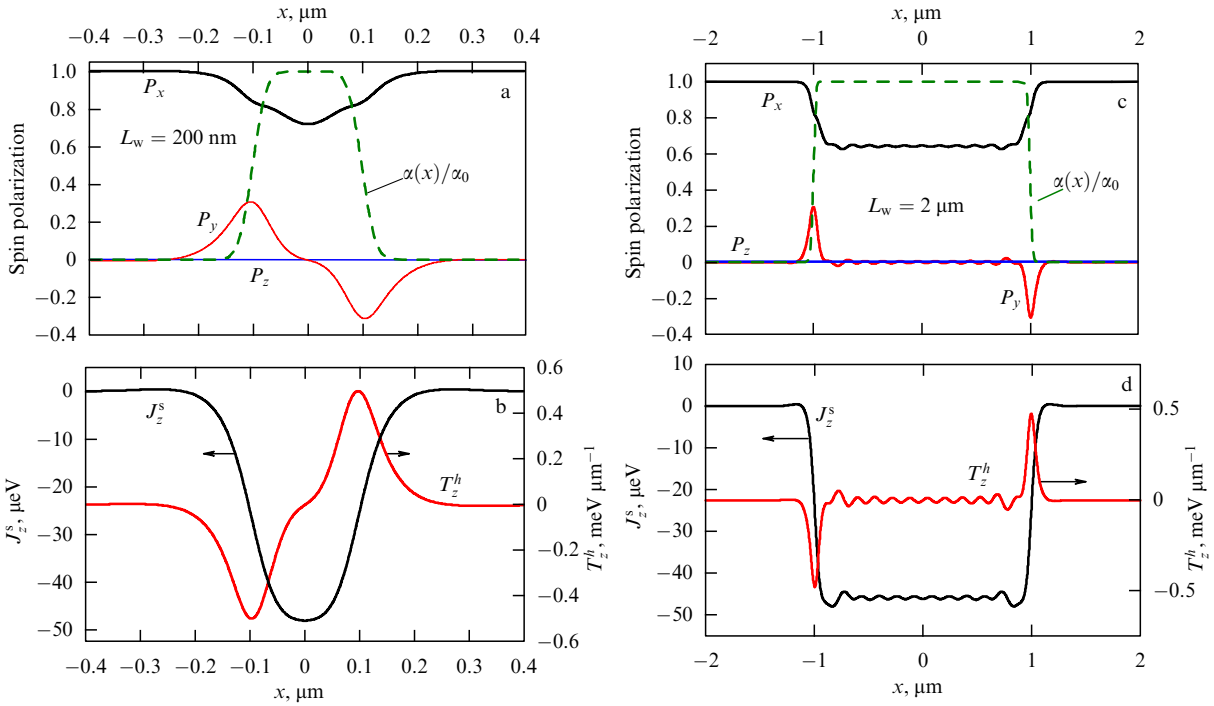

Figure 26. (a, c) Coordinate dependence of the electron spin polarization and (b, d) spin current density J_z^s and torque T_z^h exerted on an electron by a magnetic field. The coordinate axes are shown in Fig. 23a. (a, b) Nanowire length 200 nm, (c, d) nanowire length 2 μm. Parameters of the model: $\Delta_z = 0.4$ meV, $\mu = -0.2$ meV, $T = 50$ μK, $\lambda = 20$ nm, α_0 corresponds to the case $E_{SO} = 0.3$ meV, and $m^* = 0.015 m_e$ [157].

At the same time, it turns out that the spin current is directed perpendicular to the external magnetic field: $\mathbf{J}^s = (0, 0, J_z^s)$ with

$$J_z^s = -\sum_{b=\pm} \int \frac{dk_x}{2\pi} \left(\frac{\alpha}{2} + \frac{b\hbar^2}{2m^*} \frac{\alpha k_x^2}{\sqrt{(\alpha k_x)^2 + h_x^2}} \right) f\big(E_b(k_x)\big) . \tag{62}$$

This quantity can be conveniently written in the spectral decomposition form

$$J_z^s = \int dE \left(\sum_{b=\pm} J_{z,b}^s(E)\, g_b(E) \right) f(E) , \tag{63}$$

where

$$g_\pm(E) = \int \frac{dk_x}{2\pi}\, \delta\big(E - E_\pm(k_x)\big) \tag{64}$$

is the density of states of spin-up or spin-down electrons. The functions $J_{z,+}^s(E) g_+(E)$ and $J_{z,-}^s(E) g_-(E)$ are plotted in Fig. 24b, c with thin solid lines. We note that the form of $J_{z,-}^s(E) g_-(E)$ substantially depends on the magnetic field strength.

We now address effects due to the finite length of the nanowire. We assume that a nanowire of length L_w is located between two electrodes, as shown in Fig. 23b, and that the spin–orbit coupling responsible for the Rashba effect is absent in the electrodes. It then follows that α depends on the coordinate x along the nanowire. Substituting $\alpha(x)$ in the expression for the generalized Rashba Hamiltonian, Eqn (55), we obtain the following one-dimensional Hamiltonian instead of (60):

$$\hat{H}_{1D} = \frac{\hat{p}_x^2}{2m^*} - \left[\frac{\{\alpha(x), \hat{p}_x\}}{2\hbar} + h_z \right] \sigma_z - (\mathbf{h}_\perp \boldsymbol{\sigma}_\perp) . \tag{65}$$

Here, $\{\ldots\}$ is the anticommutator of the function $\alpha(x)$ and the operator $\hat{p}_x$. We can take $\alpha(x)$ to be any model function smoothly changing from zero in the domain of the electrodes to $\alpha_0 = \text{const}$ inside the nanowire. Following [157], we choose $\alpha(x)$ as

$$\alpha(x) = \frac{\alpha_0}{2} \left[\mathrm{Erf}\left(\frac{L_w/2 + x}{\sqrt{2}\lambda} \right) + \mathrm{Erf}\left(\frac{L_w/2 - x}{\sqrt{2}\lambda} \right) \right] , \tag{66}$$

where λ is the width of the domain on the electrode–nanowire border where spin–orbit coupling is turned on.

In Fig. 26, we show the coordinate dependences of the electron spin polarization $\mathbf{P}$, of the spin current projection J_z^s, and of the torque T_z^h exerted on the electron by the magnetic field, for short ($L_w = 200$ nm) and long ($L_w = 2$ μm) nanowires. The width of the domain where spin–orbit coupling turns on is $\lambda = 20$ nm in both cases. We see that taking the finite length of the nanowire into account leads to the following effects. First, near the electrode, the electrons are polarized in the y direction, perpendicular to both the external magnetic field $\mathbf{h} = (h_x, 0, 0)$ and the z axis, along which the effective field due to the spin–orbit coupling acts. A nonzero spin polarization P_y in turn gives rise to a nonzero torque $\mathbf{T}^h = \rho[\mathbf{P} \times \mathbf{h}]$ that the magnetic field produces on the electron:

$$T_z^h = -\rho P_y h_x . \tag{67}$$

Second, because the electron is localized in a domain of length L_w in a nanowire, oscillations of the spin polarization P_x and of the spin current projection J_z^s are observed. The length of these oscillations can be estimated as

$$\lambda_{osc} \approx \frac{\pi\hbar}{\sqrt{2m^*}} \left(\mu + 2E_{SO} + \sqrt{4\mu E_{SO} + 4E_{SO}^2 + \Delta_z^2} \right)^{-1/2} . \tag{68}$$

Substituting the parameters specified in the caption to Fig. 26 into formula (68), we obtain $\lambda_{\rm osc} \approx 165$ nm. For a short nanowire, it turns out that $\lambda_{\rm osc} \sim L_{\rm w}$, and oscillations are not observed. Third, we see that spin polarization penetrates from the nanowire into the bulk of the electrodes, and the penetration pattern is strongly dependent on the relation between the chemical potential μ and Δ_z [157].

We now discuss effects due to the finite width of the nanowire at a nonzero temperature. Following [164], we consider a flat nanowire with a quadratic potential along the z axis:

$$U_{\rm c}(\mathbf{r}_\perp) = -|A|\delta(y)\frac{m^*\omega^2 z^2}{2}\,. \tag{69}$$

The eigenfunctions and eigenvalues of Hamiltonian (57) are $E_{\perp,n} = \hbar\omega(2n+1)/2 + E_\delta$ and $\psi_{\perp,n}(\mathbf{r}_\perp) = \psi_n(z)\phi(y)$, where $\psi_n(z)$ are the wave functions of a one-dimensional harmonic oscillator, and $\phi(y)$ and E_δ are the wave function and the energy of a particle in a δ-shaped well. In what follows, we reference the energy to the level E_δ, i.e., we set $E_\delta = 0$. Averaging Hamiltonian (56) over the wave function $\phi(y)$, we obtain the two-dimensional Hamiltonian for the electron in a nanowire,

$$\hat{H}_{\rm 2D} = \frac{\hat{p}_x^2}{2m^*} - \frac{\alpha}{\hbar}\sigma_z\hat{p}_x + \frac{\hat{p}_z^2}{2m^*} + \frac{m^2\omega^2 z^2}{2} + \hat{H}_{\rm mix}\,, \tag{70}$$

where

$$\hat{H}_{\rm mix} = \frac{\alpha}{\hbar}\hat{p}_z\sigma_x\,. \tag{71}$$

The Hamiltonian $\hat{H}_0 = \hat{H}_{\rm 2D} - \hat{H}_{\rm mix}$ commutes with the spin projection operator σ_z, and its eigenvalues are

$$E_{0,n} = \hbar\omega\left(\frac{1}{2}+n\right) + \frac{\hbar^2}{2m^*}(k_x - \sigma k_{\rm SO})^2 - E_{\rm SO}\,, \tag{72}$$

where $n = 0, 1, 2, \ldots$ are natural numbers. We have thus obtained a set of $2n$ intersecting parabolas with minima at the points $\pm k_{\rm SO}$. The Hamiltonian $\hat{H}_{\rm mix}$ leads to a mixing of states corresponding to different values of n. If we take only the states with $n = 0, 1$ into account, we can express the lower branches of the dispersion law for the electron as [164]

$$E_{0,\sigma}(k_x) \approx E_{\rm SO} + \frac{\hbar\omega}{2} \times \left[2 + (k_x l_\omega)^2 - \sqrt{(1 - 2\sigma k_{\rm SO} k_x l_\omega^2)^2 + 2(k_{\rm SO} l_\omega)^2}\right], \tag{73}$$

where $l_\omega = \sqrt{\hbar/m^*\omega}$. The dispersion law for the electron established numerically for all possible n is shown in Fig. 27a. We can see that, because of the mixing of states with different quantum numbers n, the dispersion law is no longer parabolic. Because the number of the dispersion law branches is preserved, they still can be labeled by the quantum numbers n and σ. Specifically, curve (*1*) corresponds to the quantum numbers $n = 0$ and $\sigma = 1$, curve (*2*), to $n = 0$ and $\sigma = -1$, curve (*3*), to $n = 1$ and $\sigma = 1$, and curve (*4*), to $n = 1$ and $\sigma = -1$. However, the most interesting result of the mixing of states is that electrons acquire a nonzero spin polarization P_z (Fig. 27b). As a result, electrons moving along the nanowire in opposite directions are polarized differently, which means that the current in the nanowire is spin-polarized.

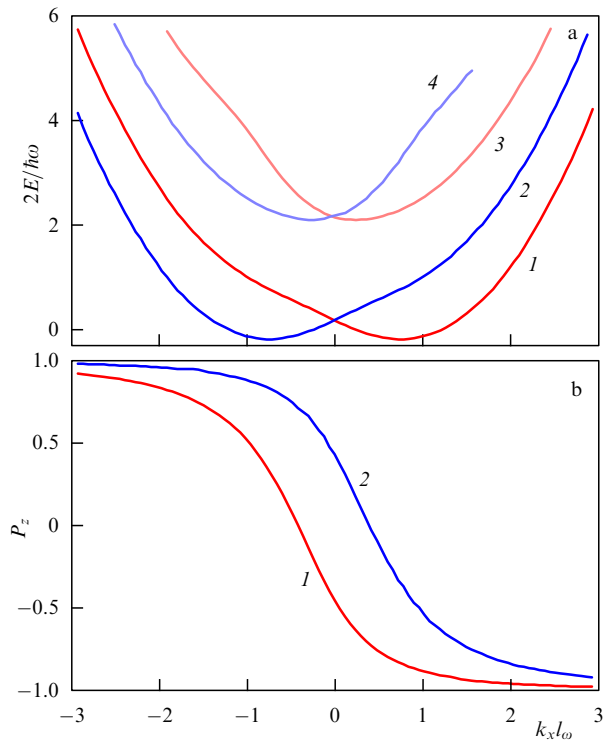

Figure 27. (a) Dispersion law $2(E(k_x) - E_{\rm SO})/\hbar\omega$ and (b) spin polarization of electrons in an infinitely long wire with the finite thickness taken into account ($k_{\rm SO} l_\omega = 0.9$) [164].

The electric current running through the nanowire can be evaluated in the ballistic regime by the Landauer formula [26, 166, 167]

$$I_{\sigma\sigma'} = \frac{2e}{h}\sum_{m=1}^{M}\int_0^\infty {\rm d}E\; T^m_{\sigma\sigma'}(E)\left[f_{\rm s}(E,\mu_{\rm s}) - f_{\rm d}(E,\mu_{\rm d})\right], \tag{74}$$

where $T^m_{\sigma\sigma'}(E)$ are the electron transmission coefficients, $f_{\rm s}(E,\mu_{\rm s})$ and $f_{\rm d}(E,\mu_{\rm d})$ are the Fermi–Dirac distribution functions with chemical potentials $\mu_{\rm s}$ and $\mu_{\rm d}$ at the source (s) and sink (d) of electrons, and σ and σ' are the spin indices of electrons at the source and at the sink. It follows from (74) that the electric current running through the nanowire can be changed by tuning the transmission coefficients $T^m_{\sigma\sigma'}(E)$. This idea underlies the operation of a nanowire field transistor [158]. A schematic of such a transistor is shown in Fig. 28a. In formula (55), two more terms must be added to the potential energy $U(\mathbf{r})$: $U_{E\|} = eE_\| x$ and $U_{E\perp} = eg(x)E_\perp y$, where $E_\|$ and $E_\perp$ are the projections of the electric field strength on the x and y axes, and $g(x)$ is a function changing smoothly from 0 to 1 at the edges of the gate. As a result, the transmission coefficients $T^m_{\sigma\sigma'}(E)$ acquire a dependence on the external electric field $E_\perp$. The Rashba effect in a nanowire leads to partial spin polarization of the electric current, with an oscillatory dependence of the transmission coefficients $T^m_{\sigma\sigma'}(E)$ on the gate voltage. This, in turn, leads to an oscillatory dependence of the total current through the nanowire on the gate voltage. In Fig. 28b, we compare theoretical [158] and experimental [165] dependences of the current through the nanowire on the gate voltage. As can be seen from the figure, theoretical and experimental data agree well in the case of a partially polarized current ($P = 0.4$).

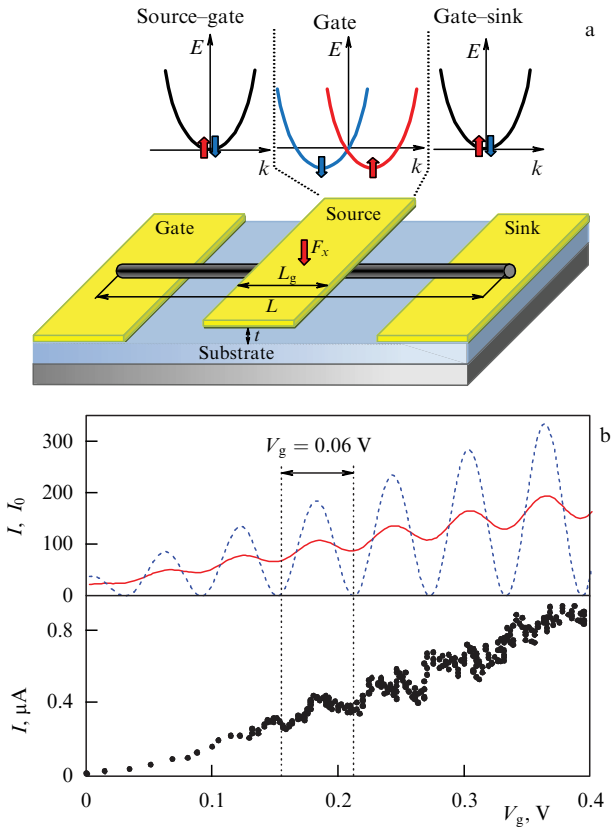

Figure 28. (a) Schematic of a field transistor based on a nanowire exhibiting the Rashba effect. (b) Current oscillations depending on the gate voltage. The upper image shows the results of theoretical calculations [158] for the totally polarized current ($P = 1$, dashed curve) and a partially polarized current ($P = 0.4$, solid curve). The lower image shows experimental results [165].

The dependence of the electric conductivity G and heat conductance K for nanowires exhibiting the Rashba effect on the longitudinal field strength $E_\parallel$ in the ballistic regime was studied in [168]. As $E_\parallel$ increases, both the electric conductivity and heat conductance of nanowires change in jumps by $G_0 = e^2/h$ (the electric conductivity quantum) and $K_0 = \pi^2 k_B^2 T/3h$ (the heat conductance quantum). Deviations from the Wiedemann–Franz law ($K/K_0 = G/G_0$) are observed only in a narrow domain near the jumps in electric conductivity. Importantly, depending on the direction of the external magnetic field, the dependences of G and K on $E_\parallel$ can be either monotonic ($\mathbf{h} = (0, 0, h_z)$) or nonmonotonic ($\mathbf{h} = (h_x, h_y, 0)$).

5.5 Magnetic properties of atomic wires and chains

The study of the magnetic properties of atomic chains is mainly motivated by the prospects of designing new-generation data storage elements [169–171]. For an atomic chain to be used as a bit of information, the time of spontaneous magnetization reversal of the chain must be sufficiently long. The possibility of producing such memory elements [172] appeared after the discovery of the gigantic magnetic anisotropy of Co atoms on a Pt(997) surface by the methods of X-ray magnetic circular dichroism [9, 173] and scanning tunneling microscopy [174–176]. Figure 29 shows the magnetization curves for atomic chains of Co on a vicinal Pt(997) surface for two values of the temperature. At a lower temperature (Fig. 29b), the atomic chains are ferromagnetic. Similar behavior is also observed for the epitaxial system Fe/Cu(111) [51, 177]. The critical temperature T_C and the spontaneous magnetization reversal time τ then increase with chain length. In accordance with the estimate in [173], a chain of 400 Co atoms can serve as a bit that is stable at room temperature. To increase the density of information recording, double or triple ferromagnetic chains could be used [178, 179]. However, experimental and theoretical work has shown that, as the width of the chain increases, the magnetic anisotropy energy (MAE) markedly decreases, approaching the MAE characteristic of monolayers [178, 180, 181]. These data are consistent with the known effect of a decrease in the MAE of atoms in a cluster as the cluster size increases [182–184].

Another way to record one bit of information is to use antiferromagnetic chains [185–188]. Antiferromagnetic chains interact more weakly with each other than ferromagnetic ones do. Therefore, the use of antiferromagnetic chains can give rise to a substantial increase in the density of information recording. The options for producing such chains and ensuring magnetization reversal in them with the help of an STM was demonstrated with the example of chains made of Fe atoms on a Cu_2N/Cu(001) surface [2, 189]. A systematic study of the chains of transition metals on the Cu_2N/Cu(001) surface has shown that they can be either ferromagnetic or antiferromagnetic [190–194]. Similar results were obtained for atomic chains on the Cu_2O/Cu(001) surface [195]. A strong increase in the stability of the bit can be ensured by using double antiferromagnetic chains [2]. In Figs 30a–c, we show STM images of double chains of Fe atoms on the Cu_2N/Cu(001) surface for temperatures of 1.6, 3.0, and 5.0 K. We see that the chain made of eight Fe atoms is in the antiferromagnetic state at a temperature below 1.2 K, and the chain of 12 Fe atoms is antiferromagnetic at a temperature below 3.0 K. In Fig. 30e on a logarithmic scale, we show the temperature dependences of the spontaneous magnetization reversal rate ν. We see that these dependences consist of two legs. At lower temperatures, $\nu = \text{const}$. That the magnetization reversal rate is independent of the temperature implies that the transition between two ground states of the chain occurs due to quantum mechanical tunneling. At higher temperatures, the dependence $\nu(T)$ is described by the classical Arrhenius law $\ln \nu \sim 1/T$, i.e., the magnetic moments of Fe atoms behave like classical vectors.

The interaction of atoms in the chain with each other, with atoms of the surface, and with the external magnetic field can be described with the effective Hamiltonian

$$H = H_{\text{exch}} + H_{\text{MAE}} + H_{\text{B}}\,, \tag{75}$$

where the first term H_{exch} describes the exchange interaction between atoms of the magnetic chain. In the lowest order in spin projections $(s_i)_\alpha$, the Hamiltonian H_{exch} is given by a quadratic form [196, 197]

$$H_{\text{exch}} = -\sum_{i>j}\sum_{\alpha\beta}(s_i)_\alpha(\hat{J}_{ij})_{\alpha\beta}(s_j)_\beta\,, \tag{76}$$

where the indices i and j label atoms and $\alpha, \beta = 1, 2, 3$. This Hamiltonian can be represented as the sum of three terms:

$$H_{\text{exch}} = -\sum_{i>j} J_{ij}(\mathbf{s}_i\,\mathbf{s}_j) + \sum_{i>j}\left(\mathbf{D}_{ij}[\mathbf{s}_i \times \mathbf{s}_j]\right) - \sum_{i>j}\sum_{\alpha\beta}(s_i)_\alpha\left(\hat{J}_{ij}^{\text{aniso}}\right)_{\alpha\beta}(s_j)_\beta\,. \tag{77}$$

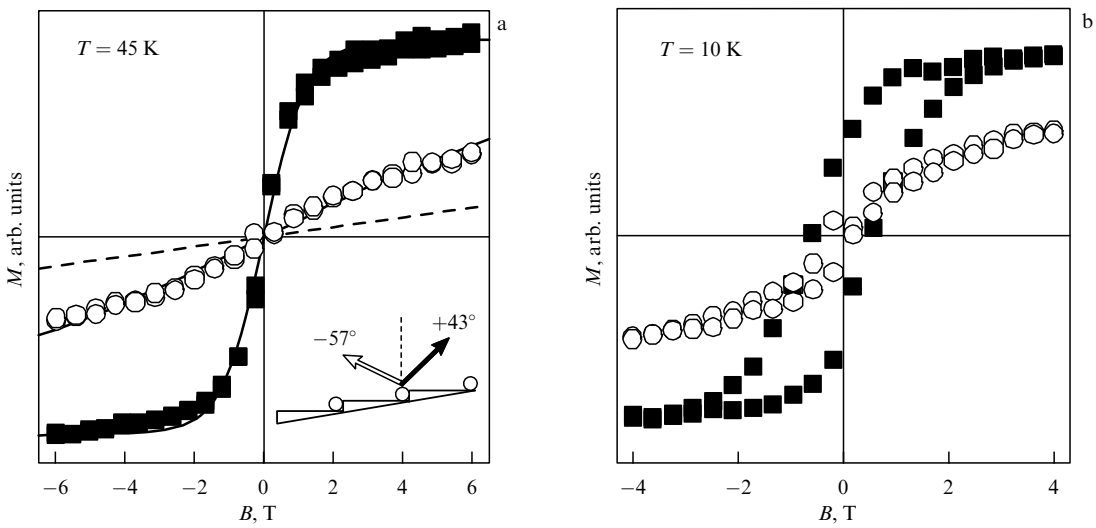

Figure 29. Surface magnetization curves for two different magnetization directions: +43° to the normal to the surface (black squares), −57° to the normal to the surface (circles) for temperatures of (a) 45 K and (b) 10 K [9].

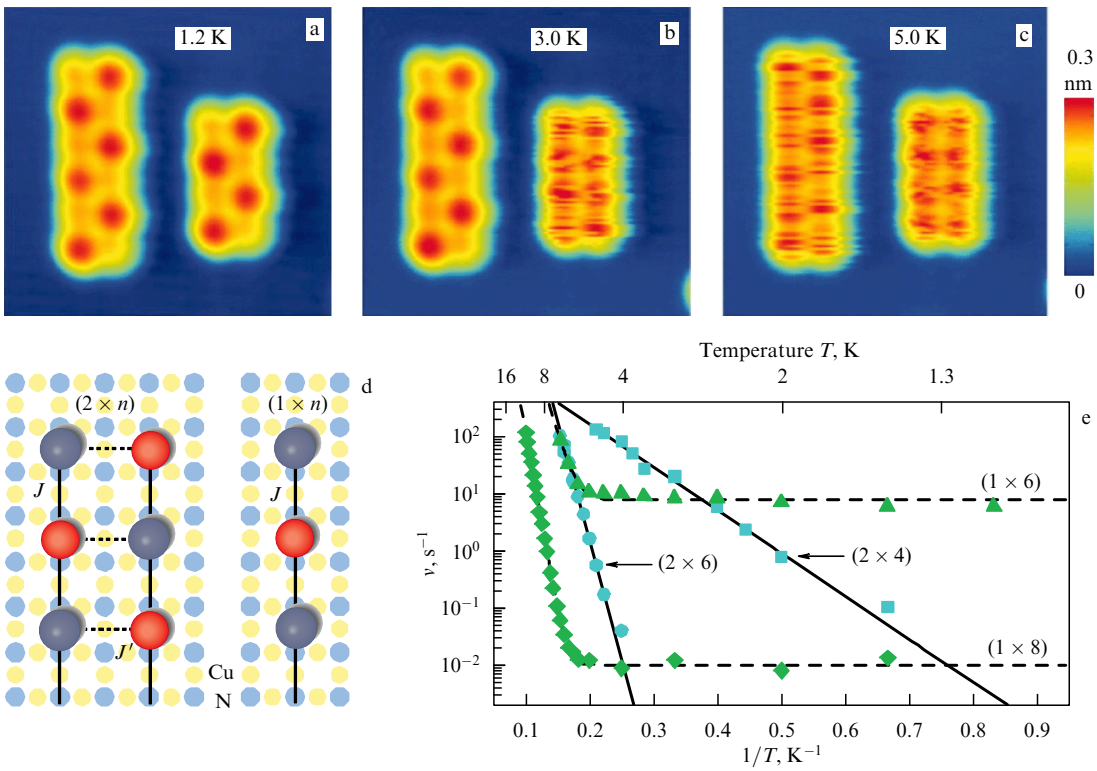

Figure 30. (a–c) Spin-polarized STM images [2] of double antiferromagnetic chains made of 12 (left) and 8 (right) Fe atoms on a $Cu_2N/Cu(001)$ surface at the respective temperatures of 1.2, 3.0, and 5.0 K. (d) Diagram of double and single-wide antiferromagnetic chains on the $Cu_2N/Cu(001)$ surface, where n is the number of atoms. (e) Dependence of the spontaneous magnetization reversal rate on the temperature.

The first term here is the standard Heisenberg Hamiltonian. The leading contribution to it is made by the exchange interaction between nearest neighbors. It can often be assumed that $J_{ij} = J(\delta_{i,j+1} + \delta_{i,j-1})$, where $J > 0$ for a ferromagnetic chain and $J < 0$ for an antiferromagnetic one. The second term in (77) is called the Dzyaloshinsky–Moriya interaction [198, 199]. In atomic chains, the Dzyaloshinsky–Moriya interaction can give rise to the formation of a spiral magnetic structure [200, 201]. The last term in (77) is the symmetric anisotropic part of the exchange interaction $((\hat{J}_{ij}^{\text{aniso}})_{\alpha\beta} = [(\hat{J}_{ij})_{\alpha\beta} + (\hat{J}_{ij})_{\beta\alpha}]/2 - J_{ij})$ and is typically less than the first two. Whenever needed, higher-order terms in $(s_i)_\alpha$ can be added to the quadratic form in (76).

The H_{MAE} term in Hamiltonian (75) describes the interaction of atoms of the chain with surface atoms and is called the magnetic anisotropy energy. In most practically relevant cases, the Hamiltonian H_{MAE} has the form

$$H_{\text{MAE}} = \sum_i \left[-K(s_i)_z^2 + E\Big((s_i)_x^2 - (s_i)_y^2 \Big) \right], \qquad (78)$$

where the z axis coincides with the easy magnetization axis. The second term in Hamiltonian (78) is related to the anisotropy of the surface on which the atomic chain is located, and is typically much less than the first term, $|E| \ll |K|$. For isotropic surfaces, $E = 0$.

The last term in Hamiltonian (75) describes the interaction of atoms in the chain with the external magnetic field and has the form

$$H_{\mathrm{B}} = -\sum_i \mu_i (\mathbf{s}_i \mathbf{B}) , \tag{79}$$

where μ_i is the magnetic moment of the ith atom of the chain and $\mathbf{B}$ is the magnetic induction of the external field.

In studying the properties of individual atoms, quantum mechanical methods are used, such as the density functional theory [179, 195, 202] and the Korringa–Kohn–Rostoker multiple scattering method [175, 203]. These methods allow evaluating all parameters of effective Hamiltonian (75). Below, we discuss the application of quantum mechanical methods to the study of the magnetic properties of chains with the example of chains made of Co and Fe atoms. It was shown in [184] that the spin magnetic moment of Fe atoms ($2.7\,\mu_{\mathrm{B}}$) immersed into the first layer of a Cu(001) surface is greater than the magnetic moment of Co atoms ($1.7\,\mu_{\mathrm{B}}$) by approximately a factor of 1.5, and the spin moments of atoms in the chains are much greater that those of adatoms. The magnetic moment increases in chains as a result of the widening of the density of d states due to the interaction of magnetic atoms with each other [183]. The spin magnetic moments do not change significantly in the course of surface relaxation and are in good agreement with the results in [183, 204], obtained without taking it into account. We note that the anisotropy of the spin magnetic moment of immersed Fe and Co atoms is negligibly small.

In contrast to the spin magnetic moment, the anisotropy of the orbital magnetic moment is quite significant [184]. For example, the orbital magnetic moment of an edge atom in a chain of four Co atoms is equal to $0.42\,\mu_{\mathrm{B}}$ for magnetization along the chain and $0.19\,\mu_{\mathrm{B}}$ for magnetization perpendicular to the plane of the surface in which the chain lies. This is because, for transition metals whose d subshell is more than half-filled, the orbital moment projection on the easy magnetization axis is typically the maximal possible [205]. The orbital magnetic moment of magnetic atoms then decreases due to their interaction with each other. Importantly, taking the surface relaxation into account leads to a sizeable decrease in the orbital magnetic moments of the immersed cobalt atoms [183].

In the Table, we list the MAE per atom, $\Delta E\,(I, z)$ $(I = x, y)$, evaluated as the difference between the total energies of all atoms in the case where the magnetic moments of magnetic atoms (Fe and Co) are directed along the I and z axes. A positive value of the MAE $\Delta E\,(I, z)$ means that magnetization of impurity atoms along the z axis is energetically advantageous; a negative value, conversely, indicates that the I axis is preferable. The MAE of immersed atoms of cobalt is 1 to 2 orders of magnitude greater than that of iron atoms located in similar chains. Similar chains made of Fe and Co atoms (except the adatoms) have different directions of the easy magnetization axes. We note the key role of copper surface relaxation in calculating the MAE of immersed nanostructures. If we ignore the surface relaxation effect and calculate the MAE assuming the Co atoms to be located at the site of an ideal crystal lattice of copper, then the MAE can increase more than twofold [183]. Even more essential differences arise when taking relaxation into account in calculating the MAE for chains made of atoms of iron. In [204], without taking surface relaxation into account, it was shown that the easy magnetization axis of linear chains immersed into the first layer of a Cu(100) surface lies in the plane of the surface perpendicular to the chains. This result explicitly contradicts the data displayed in the Table, according to which the easy magnetization axis is perpendicular to the copper surface.

Table. Average MAE values for adatoms and short chains in the first surface layer of Cu(100). All the values are expressed in meV per atom. The z axis is perpendicular to the surface; the x and y axes lie in the plane of the surface, with the x axis directed along the chain [184].

Configuration	$\Delta E_{\mathrm{Fe}}(x, z)$	$\Delta E_{\mathrm{Fe}}(y, z)$	$\Delta E_{\mathrm{Co}}(x, z)$	$\Delta E_{\mathrm{Co}}(y, z)$
Adatom	−0.11	−0.11	−2.01	−2.01
Dimer	0.14	0.10	−1.71	−1.11
Trimer	0.06	0.04	−1.59	−0.94
Tetramer	0.05	0.03	−1.68	−1.09

Knowing the individual magnetic properties of atoms, we can pass to considering collective magnetic properties of chains, as these follow from Hamiltonian (75). We do not discuss the properties of infinitely long chains, which have been studied and expounded on in a number of textbooks, monographs, and review papers, but concentrate instead on those properties of finite-length chains that can be derived experimentally. The length of such chains is typically under 100 atoms. We note that, due to the finiteness of the length of magnetic chains, the original assumptions of several fundamental theorems no longer hold, including the Mermin–Wagner theorem [206] on the absence of ferromagnetism and antiferromagnetism in one- and two-dimensional isotropic Heisenberg models. This opens up a number of options for the practical use of finite-length magnetic chains.

Theoretical methods for studying the magnetic properties of chains can be divided into three large classes: (1) various quantum mechanical methods; (2) classical magnetic dynamics in the framework of the Landau–Lifshitz–Gilbert approximation; and (3) classical statistical methods based on the Monte Carlo method.

In studying the properties of magnetic chains with quantum mechanical methods, $(s_i)_\alpha$ must be understood as spin projection operators of the ith atom on the $\alpha = x, y, z$ axes. The methods then essentially depend on the substrate underlying the atomic chain. As a rule, an insulator (or semiconductor) or normal-state metal crystal is used as a substrate. [1]

If a magnetic chain is placed on an insulator or semiconductor surface, the contribution of the MAE to Hamiltonian (75) is small and can be neglected. The atomic chain can thus be considered a closed system, and its dynamics can be described using the formalism of wave functions. From the practical standpoint, an interesting result is the possibility of using atomic chains for quantum transmission of information [208, 209]. The accuracy of information transmission from one end of the chain to the other decreases fairly slowly with the chain length, $\sim N^{-1/3}$, where N is the number of magnetic atoms in the chain. Another interesting phenomenon is the electromagnetic dipole radiation by the spin-flip wave in a magnetic chain

[1] We do not discuss the properties of magnetic chains on superconductor surfaces here (see review paper [207] and references therein).

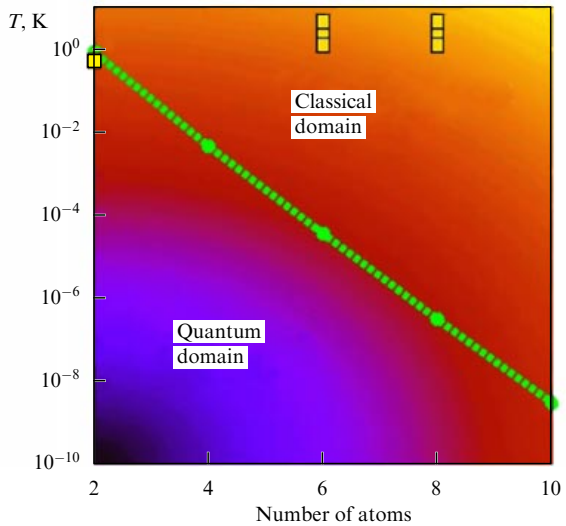

Figure 31. Temperature–number-of-atoms diagram for Fe chains on a $Cu_2N/Cu(001)$ surface [211]. The dotted line separates the domain where magnetization reversal occurs as a result of quantum mechanical oscillations and where it occurs classically. The dots are experimental values from [2, 212].

[210]. It then turns out that, with the quantum fluctuations of the field taken into account, the radiation energy flux is much higher than the energy flux in the averaged electromagnetic field.

If the magnetic chain is placed on a metal surface, the chain atoms strongly interact with the surface electron gas. In this case, the magnetic chain is part of the chain + surface system, and its state must be described in the language of density matrices rather than wave functions. The density matrix ρ of a magnetic chain is a solution of the Lindblad equation [211, 213]

$$\frac{\partial \rho}{\partial t} = -\frac{\mathrm{i}}{\hbar}\left[H_{\mathrm{eff}}, \rho\right] + L\left[\rho\right], \tag{80}$$

where $L[\rho]$ is the Lindblad superoperator. A systematic derivation of Eqn (80) and analysis of its compatibility with the laws of thermodynamics are available in [214]. In the case of antiferromagnetic chains of Fe on a $Cu_2N/Cu(001)$ surface, interaction with the substrate leads to the suppression of quantum mechanical oscillations (Rabi oscillations) between the two ground states of the antiferromagnetic chain [211]. As a result, magnetization reversal of the chains occurs in a classical manner, i.e., due to the flip of magnetic moments, by overcoming an activation barrier. The transition between classical and quantum mechanical regimes of magnetization reversal depends on the temperature and the chain length (Fig. 31). As can be seen from Fig. 31, quantum properties of magnetic chains manifest themselves only at low temperatures of ~ 1 K. At the same time, from the standpoint of practical applications, the magnetic dynamics of chains at higher temperatures are of interest. It was shown in [215] that, in the classical limit, the dynamics of a magnetic chain can be described by the Landau–Lifshitz–Gilbert equation [202, 216, 217]

$$\frac{\partial \mathbf{s}_i}{\partial t} = -\gamma\left[\mathbf{s}_i \times \mathbf{H}_i^{\mathrm{eff}}\right] + \frac{\alpha}{\mu_i}\left[\mathbf{s}_i \times \frac{\partial \mathbf{s}_i}{\partial t}\right], \tag{81}$$

where $\mathbf{s}_i$ is the unit (classical) vector of the magnetic moment of the ith atom of the chain, γ is the gyromagnetic factor, α is the damping constant, and $\mathbf{H}_i^{\mathrm{eff}}$ is the effective magnetic field strength acting on the ith atom:

$$\mathbf{H}_i^{\mathrm{eff}} = -\frac{1}{\mu_i}\frac{\partial H}{\partial \mathbf{s}_i}. \tag{82}$$

Here, H is the effective Hamiltonian (75) of the magnetic chain.

It must be kept in mind that this interpretation of Eqn (81) is different from the original interpretation of Landau and Lifshitz. In the macroscopic derivation of Eqn (81), it is assumed that $\mathbf{s}$ is a unit vector of magnetization of a macroscopically small volume of a ferromagnet, which nevertheless contains a large number of atoms. On the other hand, we here assume that $\mathbf{s}_i$ is the unit vector of the magnetic moment of a single atom [202, 215].

Equation (81) is especially useful in modeling the dynamics of magnetization reversal of short ferromagnetic and antiferromagnetic chains in an external magnetic field. As an example, we consider the magnetization reversal of an antiferromagnetic chain made of three Fe atoms on the $Cu_2N/Cu(001)$ surface under the action of an STM tip and of an external magnetic field [202]. The STM tip is modeled with the help of a fourth Fe atom placed at a distance $\Delta = 5$ Å from the chain atoms. The external magnetic field is a superposition of a constant magnetic field H_z perpendicular to the surface (along the easy magnetization axis) and the pulsed field $H_{\mathrm{pls}}(t)$ directed along the chain. In this case, the pulsed field is necessary for activating the magnetization reversal of the chain. It is given by a rectangular pulse 0.3 T in amplitude ($H_{\mathrm{pls}} \ll H_z$) and 0.3 ps in duration. In Fig. 32, we show the dynamics of the flip of the edge atom in a chain. The magnetization reversal time of the chain is 200 to 400 ps, and the minimal field H_z necessary for magnetization reversal depends on the position of the STM tip.

In the considered example, magnetization reversal of all three Fe atoms occurs simultaneously. In longer chains, made of tens or hundreds of atoms, a magnetization reversal mechanism accompanied by the formation of domain walls can be energetically advantageous. It can then be assumed that the magnetic moments of the atoms flip at random. If we assume that the flip of magnetic moments is a Markov process, we can construct a KMCM for magnetic moments. We consider the KMCM [218] for a special case of the effective Hamiltonian (75):

$$H = -\sum_{i>j} J_{ij}(\mathbf{s}_i\,\mathbf{s}_j) - K\sum_i (\mathbf{s}_i\,\mathbf{e})^2 - \mu\sum_i (\mathbf{s}_i\,\mathbf{B}), \tag{83}$$

where $\mathbf{s}_i$ and $\mathbf{e}$ are the respective unit vectors of the magnetic moment of atoms and of the easy magnetization axis, μ is the modulus of the magnetic moment of an atom, K is the MAE, and $J_{ij} = J(\delta_{i,j+1} + \delta_{i,j-1})$ is the exchange integral. For a ferromagnetic chain, $J > 0$, and for an antiferromagnetic one, $J < 0$. We assume that the external magnetic field $\mathbf{B}$ is applied along the easy magnetization axis $\mathbf{e}$. Then, the magnetic moments of the atoms can be aligned either parallel or antiparallel to the easy magnetization axis, $(\mathbf{s}_i\,\mathbf{e}) = \pm 1$. The magnetic moment of the atom is then directed up if $(\mathbf{s}_i\,\mathbf{e}) = 1$ and down if $(\mathbf{s}_i\,\mathbf{e}) = -1$.

The flip of the ith magnetic moment can occur in two different ways. If $2K > h_i$, where $h_i = \sum_j J_{ij}(\mathbf{s}_i\,\mathbf{s}_j) + \mu(\mathbf{s}_i\,\mathbf{B})$, there is an energy barrier between the initial and the final states of the chain (Fig. 33a–c), and the magnetic moment flip rate is given by

$$\nu_i = \nu_0 \exp\left(-\frac{(2K + h_i)^2}{4Kk_{\mathrm{B}}T}\right), \tag{84}$$

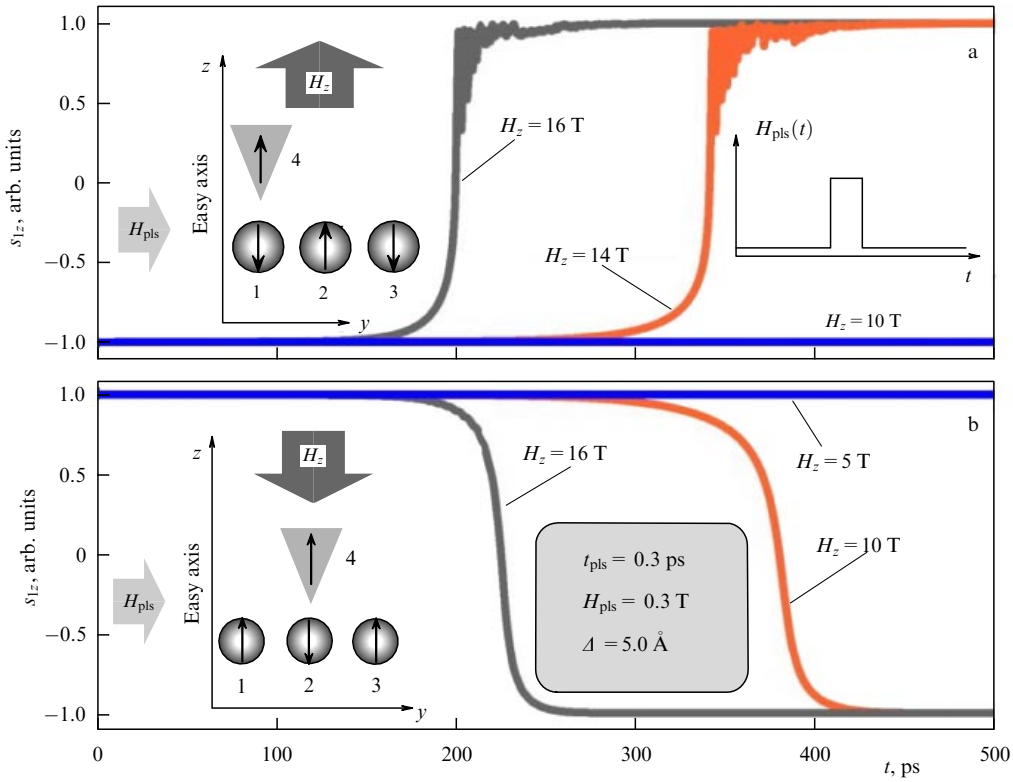

Figure 32. Magnetization reversal dynamics for a chain made of three Fe atoms on a $Cu_2N/Cu(001)$ surface under the action of an STM tip and an external magnetic field. For clarity, the dependence of the s_z projection for the edge atom in the chain is shown. Two positions of the STM tip are (a) above the edge atom, (b) above the middle atom [202].

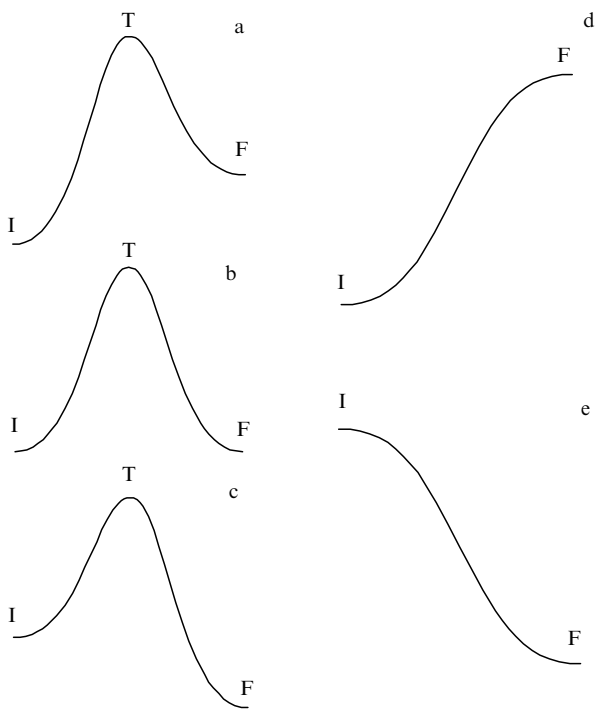

Figure 33. Via a flip of a single magnetic moment from the initial position (I) to the final position (F), the chain energy can change in two ways: (a–c) via a saddle point (T) and (d, e) without overcoming an energy barrier. (Adapted from [218].)

where k_B is the Boltzmann constant, T is the temperature of the system, and v_0 is a frequency prefactor. But, if $2K \leqslant h_i$, then the energy barrier between the $(\mathbf{s}_i\,\mathbf{e}) = \pm 1$ states is absent (Fig. 33d, e), and the magnetic moment flip rate can be calculated as [219]

$$v_i = v_0 \frac{\exp\left(-2h_i/k_B T\right)}{1 + \exp\left(-2h_i/k_B T\right)} \,. \tag{85}$$

For chains made of transition metal atoms placed on a metal substrate, the frequency prefactor v_0 is 10^9 Hz by the order of magnitude [9].

The proposed KMCM model can be used to estimate the critical temperature T_C and the magnetization reversal time of the chain τ, to construct magnetization curves for chains, and to find the coercive force [220–226]. As an example, in Fig. 34a, b, we show magnetization curves of a chain made of 80 Co atoms on a Pt(997) surface at temperatures of 10 and 45 K. Here, $M \in [-1, 1]$ is the mean magnetization of the chain (in arbitrary units), averaged over 500 magnetization reversal cycles. We can see that, at 45 K, the coercive force is close to zero. But the chain remains ferromagnetic, as can be seen from the slope of the magnetization curve at $M = 0$ at both temperature values. The temperature dependence of the coercive force for chains made of 10 and 80 Co atoms is shown in Fig. 34c. This dependence is approximated well by the formula

$$B_c = A \exp\left[-\left(\frac{T}{T_0}\right)^p\right], \tag{86}$$

where T_0 is some temperature below the critical temperature T_C. The critical temperature T_C of the ferromagnetic chain can be estimated from a plot of the mean magnetization

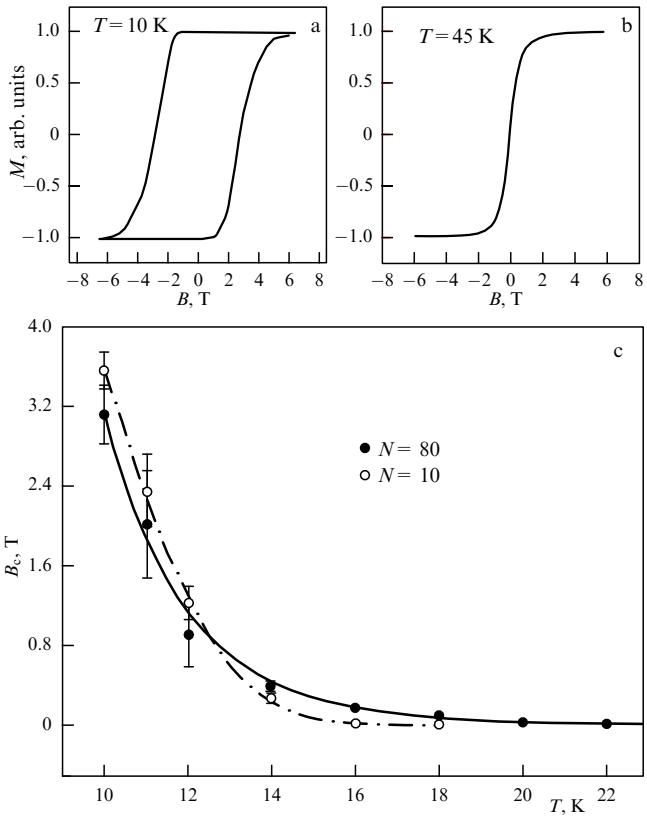

Figure 34. Magnetization curves for a chain of 80 Co atoms on a Pt(997) surface in accordance with KMCM modeling results [218] at the temperature of (a) 10 K and (b) 45 K. (c) Temperature dependence of the coercive force for chains made of 10 and 80 Co atoms.

modulus $|M|$ as a function of the temperature T. The critical temperature T_C is then determined as the inflection point on the plot of $|M|(T)$ [224, 225]. The same can be done for antiferromagnetic chains, but with the order parameter chosen as the modulus of the difference between magnetizations of two sublattices, $|M_1 - M_2|$ [226]. The critical temperature can be found in this way, because the order parameter is nonvanishing at any temperature for finite-length chains.

When the parameters J and K differ negligibly for different atoms in the chain, the KMCM model can be used to construct a simple analytic procedure for calculating the magnetization reversal time τ for ferromagnetic and antiferromagnetic chains [227, 228]. At temperature $T \ll T_C$, the magnetic moments of all atoms in the chain are aligned most of the time. For definiteness, we assume that all magnetic moments are directed up. A magnetic moment flip inside the chain has a low probability at low temperatures. Therefore, the magnetization reversal of the chain starts with a flip of the magnetic moment of one of the edge atoms, which means that a domain wall emerges at the edge of the chain. If this domain wall propagates to the opposite edge of the chain, the magnetic moments of all atoms in the chain are directed down, i.e., the chain reverses its magnetization. If the temperature is sufficiently low, then a second domain wall does not appear within the time the first domain wall travels along the chain. The problem of finding magnetization reversal of a finite-length atomic chain thus reduces to the problem of a random walk of one domain wall. If the chain consists of N atoms, the domain wall can be in one of the $N-1$ positions between atoms $i = 1, \ldots, N-1$. If the magnetic moments of all atoms are directed up or down, we assign the domain wall the position $i = 0$ or $i = N$. To solve the problem of random walk of the domain wall, we use the mean-rate method, known to work well in studying random walks of atoms [229, 230].

We first consider magnetization reversal of an atomic chain in the absence of an external field, $\mathbf{B} = 0$. The random walk of the domain wall is then characterized by only three rates: the rate ν_1 of domain wall formation at the chain end, the rate ν_2 of domain wall disappearance at the chain end, and the rate ν_3 of domain wall displacement to a neighboring position inside the chain; all three can be evaluated from formulas (84) and (85).

We let $\nu_{i\to j}$ denote the rate of domain wall displacement from position i to position $j = i \pm 1$; then, $\nu_{0\to 1} = \nu_{N\to N-1} = \nu_1$, $\nu_{1\to 0} = \nu_{N-1\to N} = \nu_2$, and $\nu_{1\to 2} = \nu_{2\to 1} = \ldots = \nu_{N-2\to N-1} = \nu_{N-1\to N-2} = \nu_3$. We let τ_i^1 denote the mean time that the domain wall resides in the ith position. Evidently, $\tau_0^1 = \tau_N^1 = 1/\nu_1$, $\tau_1^1 = \tau_{N-1}^1 = 1/(\nu_2 + \nu_3)$, and $\tau_2^1 = \ldots = \tau_{N-2}^1 = 1/2\nu_3$.

We assume that, at the initial instant, the domain wall was in position $i = 0$. We must evaluate the mean time that the domain wall takes to move to position $i = N$. To do so, we introduce the $N \times N$ transition matrix T with the elements

$$T_{ij} = \tau_j^1 \nu_{j\to i} \,. \tag{87}$$

Because the domain wall is in position $i = 0$ at the initial instant, the probability of finding it in the first N positions is $P_i^{\text{init}} = \delta_{0i}$. The probability P_i of finding the domain wall in position i after a large number of random moves can be found from the system of linear equations

$$\sum_{j=0}^{N-1} (\delta_{ij} - T_{ij}) P_j = P_i^{\text{init}} \,. \tag{88}$$

Using the explicit form of the T matrix, it is easy to solve the system of linear equations (88). The total random walk time for the domain wall is

$$\tau_{\text{tot}} = \sum_{i=0}^{N-1} \tau_i^1 P_i \,. \tag{89}$$

In finding τ_{tot}, we assumed that the domain wall appears in position $i = 0$. But it can appear on both ends of the atomic chain with equal probability, and therefore the mean magnetization reversal time τ for the chain must be half the time τ_{tot}. From (88) and (89), after simple calculations, we find

$$\tau = \frac{1}{2a} \left\{ \frac{a}{\nu_3} \left(\frac{N-1}{2} \right) \left[N - \frac{2(1-2a)}{1-a} \right] + \frac{1}{\nu_1} \left[N(1-a) - 2(1-2a) \right] \right\} , \tag{90}$$

where $a = \nu_3/(\nu_2 + \nu_3)$. Expression (90) is valid not only for long ($N \gg 1$) but also for relatively short ($N \sim 10$) chains if the condition $KN - 2J \gg k_B T$ is satisfied, which ensures that the probability of domain wall formation is much higher than the probability of a simultaneous flip of all magnetic moments.

We generalize formula (90) to the case of a nonvanishing external magnetic field. Random walk of the domain wall is

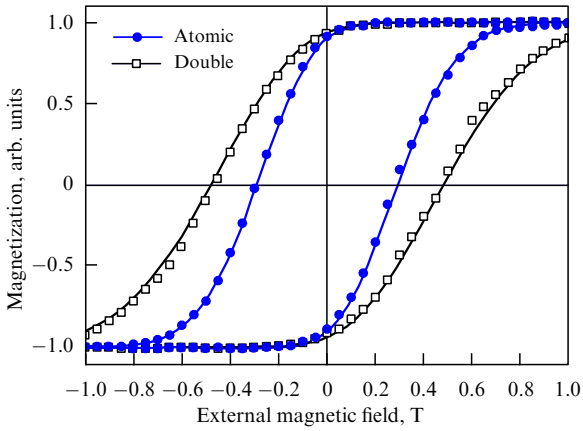

Figure 35. Magnetization curves of atomic and double ferromagnetic chains of Co on a Pt(997) surface [231]. The effective Hamiltonian parameters are $N = 100$, $J = 7.5$ meV, $K = 2.0$ meV, $\mu = 2.4\,\mu_{\rm B}$, and $T = 16$ K for the atomic chain; $2N = 200$, $J = J' = 7.5$ meV, $K = 0.34$ meV, $\mu = 2.4\,\mu_{\rm B}$, and $T = 40$ K for the double chain. The rate of change of the external magnetic field is $|{\rm d}B/{\rm d}t| = 130$ T s^{-1} in both cases. Dots show the results of KMCM modeling, averaged over 1000 cycles of magnetization reversal, and solid lines show solutions to the Cauchy problem (93).

now characterized not by three but by six frequencies: $\nu_{1\pm}$, $\nu_{2\pm}$, and $\nu_{3\pm}$. Repeating the above calculations, we obtain

$$\tau(B) = \frac{1}{2(1-a_-)}\left\{\frac{a_-}{\nu_{3-}} + \frac{(N-2)(1-a_-)+(a_--\alpha)S_{N-2}}{\nu_{3+}(1-\alpha)} + \frac{S_{N-2}-(a_-+\alpha a_+)S_{N-3}+\alpha a_+ a_- S_{N-4}}{\nu_{1+}a_+}\right\}, \qquad (91)$$

where $\alpha = (1-)/b$, $S_N = (1-\alpha^N)/(1-\alpha)$, $a_+ = \nu_{3+}/(\nu_{2-}+\nu_{3+})$, $a_- = \nu_{3-}/(\nu_{2+}+\nu_{3-})$, and $b = \nu_{3+}/(\nu_{3-}+\nu_{3+})$. In the limit $B \to 0$, formula (91) becomes formula (90).

Formula (91) can be used to study magnetodynamical properties of atomic chains at temperatures below $T_{\rm max}$. If the magnetic induction B depends on time, $B = B(t)$, then the magnetization reversal rates of the atomic chain also depend on time: $\nu_{\uparrow\to\downarrow}(t) = 1/\tau(B(t))$ and $\nu_{\downarrow\to\uparrow}(t) = 1/\tau(-B(t))$. The probability of finding the chain in a state where magnetic moments of all atoms are directed up is to be found from the master equation

$$\frac{{\rm d}P_\uparrow}{{\rm d}t} = P_\downarrow \nu_{\downarrow\to\uparrow} - P_\uparrow \nu_{\uparrow\to\downarrow}\,, \qquad (92)$$

where $P_\uparrow + P_\downarrow = 1$. If the atomic chain magnetization is measured in dimensionless units $M \in [-1, 1]$, then $M = P_\uparrow - P_\downarrow$, and Eqn (92) implies an equation for the atomic chain magnetization

$$\frac{{\rm d}M(t)}{{\rm d}t} = \mathfrak{A}(t)M(t) + \mathfrak{B}(t)\,, \qquad (93)$$

where $\mathfrak{A} = -\nu_{\uparrow\to\downarrow} - \nu_{\downarrow\to\uparrow}$ and $\mathfrak{B} = \nu_{\downarrow\to\uparrow} - \nu_{\uparrow\to\downarrow}$. Equation (93), taken together with the initial condition $M(0) = M_0$, is a Cauchy problem, which is to be solved numerically.

The described method can be generalized to the case of double ferromagnetic or antiferromagnetic chains [231, 232]. The exchange interaction between atoms inside the chain is then described by an exchange integral J, and the interaction between atoms of neighboring chains, by an exchange integral J' (Fig. 30d) in the case of both weak ($J'N \lesssim J$) and strong ($J' \ln N \gtrsim J$) coupling between the chains. The results obtained from analytic formulas are in good agreement with the results of KMCM modeling. In Fig. 35, we show magnetization curves of atomic and double ferromagnetic chains of Co on a Pt(997) surface. We see that the results of KMCM modeling and of the numerical solution of Cauchy problem (93) practically coincide. The analytic method expounded above does not require collecting statistics and therefore allows constructing magnetization curves much more quickly than the KMCM modeling does.

6. Conclusions

The analysis of extensive experimental data performed in this review has shown that, among numerous epitaxial systems, the most promising ones as regards the formation of atomic chains are metallic vicinal stepped surfaces and the surfaces of metals and semiconductors with low Miller indices. The formation and evolution of atomic chains and wires have been described using simple theoretical models. The conditions for growing one-dimensional structures are shown to depend on both the epitaxial system and external parameters. Studies by the kinetic Monte Carlo method have shown that the transition from one equilibrium state to another under heating or cooling occurs via nonequilibrium states, and therefore the distribution of lengths of such structures depends on the duration of the experiment. By controlling the annealing time and temperature, we can control the sizes, and therefore the properties, of one-dimensional atomic structures.

The study of the electronic and magnetic properties of atomic chains has revealed a number of physical processes and phenomena that are important for designing new methods of information storage and transmission. In atomic wires with the gigantic Rashba effect in a nonvanishing magnetic field directed along the wire, electrons are polarized in the magnetic field direction. Taking the finite length of the wire into account then leads to the following effects: (1) near the electrodes, electrons are polarized in the direction perpendicular to both the external magnetic field and the axis along which the effective field acts due to the spin–orbit coupling; (2) oscillations of spin polarization and of the spin current projection are observed; (3) spin polarization penetrates from the wire into the bulk of the electrodes. As the temperature increases, states with different quantum numbers mix, which leads to the appearance of the spin polarization current running through the wire, even in the absence of a magnetic field. In addition, the current running through the wire can be changed using an external electric field directed perpendicular to the nanowire. These properties of atomic wires with the gigantic Rashba effect can be used in designing various devices such as field transistors.

We especially note theoretical studies of the magnetic properties of atomic chains and wires. This is because only theoretical approaches allow proceeding from the knowledge of the individual magnetic properties of atoms to the consideration of collective magnetic properties of chains, and subsequently assessing their prospects for practical applications. Theoretical methods for studying the magnetic properties of atomic chains can be divided into three large classes: (1) quantum mechanical methods, (2) classical magnetic dynamics in the framework of the Landau–Lifshitz–Gilbert approximation, and (3) classical statistical methods based on the Monte Carlo method. Each next class, being a

rough approximation of the preceding one, allows studying the properties of longer chains over longer time intervals.

Our results of studying the magnetic properties of atomic chains suggest their strong dependence on the material of the substrate. Typically, the substrate is made of a crystal of an insulator, a semiconductor, or a normal-state metal. If the magnetic moments of the chains weakly interact with insulator substrates, then such atomic chains can be used for the quantum transmission of information. Conversely, the interaction of atoms in the chain with metallic substrates can lead to the appearance of gigantic magnetic anisotropy, which is promising as regards designing new-generation information storage devices, where a bit of information can represented by both ferromagnetic and antiferromagnetic atomic chains.

The authors are grateful to all of their colleagues at Lomonosov Moscow State University. They are also grateful to the Russian Science Foundation (grant 21-72-20034). S V Kolesnikov contributed only to Sections 5.4 and 5.5. This work was supported by the Russian Foundation for Basic Research within research projects 19-12-50010 (Ekspansiya) and 19-32-90045, and also by the BASIS foundation for support of theoretical physics and mathematics.

References

1. Hirjibehedin C F, Lutz C P, Heinrich A J *Science* **312** 1021 (2006)
2. Loth S et al. *Science* **335** 196 (2012)
3. Fölsch S et al. *Phys. Rev. Lett.* **92** 056803 (2004)
4. Gambardella P et al. *Phys. Rev. B* **61** 2254 (2000)
5. Gambardella P et al. *Surf. Sci.* **449** 93 (2000)
6. Schoiswohl J et al. *Phys. Rev. Lett.* **97** 126102 (2006)
7. Surnev S et al. *ChemPhysChem.* **11** 2506 (2010)
8. Zaki N et al. *Phys. Rev. B* **80** 155419 (2009)
9. Gambardella P et al. *Nature* **416** 301 (2002)
10. Himpsel F J, Ortega J E *Phys. Rev. B* **50** 4992(R) (1994)
11. Yan L et al. *Appl. Phys. Lett.* **86** 102503 (2005)
12. Ferstl P et al. *Phys. Rev. Lett.* **117** 046101 (2016)
13. Giovanardi C et al. *Phys. Rev. B* **78** 205416 (2008)
14. Yeom H W et al. *Phys. Rev. Lett.* **82** 4898 (1999)
15. Himpsel F J et al. *J. Phys. Condens. Matter* **13** 11097 (2001)
16. Zandvliet H J W, van Houselt A, Poelsema B *J. Phys. Condens. Matter* **21** 474207 (2009)
17. Watanabe T et al. *Surf. Sci.* **653** 71 (2016)
18. Zhang L et al. *Appl. Surf. Sci.* **439** 101 (2018)
19. Stekolnikov A A et al. *Phys. Rev. Lett.* **100** 196101 (2008)
20. Mocking T F et al. *Nat. Commun.* **4** 2387 (2013)
21. Kabanov N S et al. *Appl. Surf. Sci.* **404** 12 (2017)
22. Schäfer J et al. *Phys. Rev. Lett.* **101** 236802 (2008)
23. Oncel N et al. *Phys. Rev. Lett.* **95** 116801 (2005)
24. Schaefer J et al. *New J. Phys.* **11** 125011 (2009)
25. Aulbach J et al. *Phys. Rev. Lett.* **111** 137203 (2013)
26. Datta S *Electronic Transport in Mesoscopic Systems* (Cambridge: Cambridge Univ. Press, 1995)
27. Klavsyuk A L, Saletsky A M *Phys. Usp.* **58** 933 (2015); *Usp. Fiz. Nauk* **185** 1009 (2015)
28. Crain J N, Pierce D T *Science* **307** 703 (2005)
29. Erwin S C, Himpsel F J *Nat. Commun.* **1** 58 (2010)
30. Park J et al. *Phys. Rev. Lett.* **110** 036801 (2013)
31. Gambardella P et al. *Phys. Rev. B* **73** 245425 (2006)
32. Yilmaz M B, Zimmermann F M *Phys. Rev. E* **71** 026127 (2005)
33. Tokar V I, Dreyssé H *Phys. Rev. B* **76** 073402 (2007)
34. Petrov P et al. *Appl. Math. Model.* **35** 1331 (2011)
35. Tokar V I, Dreyssé H *Phys. Rev. E* **92** 062407 (2015)
36. Kocán P et al. *Phys. Rev. E* **80** 061603 (2009)
37. Syromyatnikov A G, Saletsky A M, Klavsyuk A L *Phys. Rev. B* **97** 235444 (2018)
38. Syromyatnikov A G, Saletsky A M, Klavsyuk A L *JETP Lett.* **110** 348 (2019); *Pis'ma Zh. Eksp. Teor. Fiz.* **110** 331 (2019)
39. Syromyatnikov A G, Saletsky A M, Klavsyuk A L *Surf. Sci.* **693** 121528 (2020)
40. Syromyatnikov A G, Saletsky A M, Klavsyuk A L *J. Magn. Magn. Mater.* **510** 166896 (2020)
41. Ovesson S et al. *Phys. Rev. B* **64** 125423 (2001)
42. Zaum C et al. *Phys. Rev. Lett.* **114** 146104 (2015)
43. Kim S Y, Lee I H, Jun S *Phys. Rev. B* **76** 245407 (2007)
44. Mińkowski M, Zaluska-Kotur M A *Surf. Sci.* **642** 22 (2015)
45. Fichthorn K A, Scheffler M *Phys. Rev. Lett.* **84** 5371 (2000)
46. Kuhnke K, Kern K *J. Phys. Condens. Matter* **15** S3311 (2003)
47. Kolesnikov S V "Issledovanie samoorganizatsii nanostruktur na poverkhnosti medi" ("Investigation of the self-organization of nanostructures on the copper surface"), PhD Thesis (Phys.-math. sciences) (Moscow: Lomonosov Moscow State Univ., 2010)
48. de la Figuera J et al. *Appl. Phys. Lett.* **66** 1006 (1995)
49. Chang H W et al. *J. Appl. Phys.* **100** 084304 (2006)
50. Vu Q H, Morgenstern K *Phys. Rev. B* **95** 125423 (2017)
51. Shen J et al. *Phys. Rev. B* **56** 2340 (1997)
52. Guo J et al. *Phys. Rev. B* **73** 193405 (2006)
53. Prieto J E, de la Figuera J, Miranda R *Phys. Rev. B* **62** 2126 (2000)
54. Speller S et al. *Surf. Sci.* **405** L542 (1998)
55. de la Figuera J et al. *Surf. Sci.* **307–309** 538 (1994)
56. de la Figuera J et al. *Phys. Rev. B* **47** 13043 (1993)
57. Mo Y et al. *Phys. Rev. Lett.* **94** 155503 (2005)
58. Negulyaev N N et al. *Phys. Rev. B* **77** 085430 (2008)
59. Cochrane W *P. Phys. Soc.* **48** 723 (1936)
60. Pedersen M et al. *Surf. Sci.* **387** 86 (1997)
61. Zaki N et al. *Phys. Rev. B* **87** 161406 (2013)
62. Syromyatnikov A G et al. *J. Exp. Theor. Phys.* **124** 139 (2017); *Zh. Eksp. Teor Fiz.* **151** 160 (2017)
63. Syromyatnikov A G, Klavsyuk A L, Saletsky A M *JETP Lett.* **100** 24 (2014); *Pis'ma Zh. Eksp. Teor. Fiz.* **100** 26 (2014)
64. Ding H F et al. *Phys. Rev. B* **76** 033409 (2007)
65. Bellisario D O et al. *J. Phys. Chem. C* **113** 12863 (2009)
66. Syromyatnikov A, Klavsyuk A, Saletsky A *IEEE Magn. Lett.* **10** 6111003 (2019)
67. Röder H et al. *Nature* **366** 141 (1993)
68. York S M, Leibsle F M *Phys. Rev. B* **64** 033411 (2001)
69. Wang J T et al. *Phys. Rev. Lett.* **105** 116102 (2010)
70. Simov K R, Nolph C A, Reinke P *J. Phys. Chem. C* **116** 1670 (2012)
71. Liu H, Reinke P *Surf. Sci.* **602** 986 (2008)
72. Nolph C A, Liu H, Reinke P *Surf. Sci.* **605** L29 (2011)
73. Liu H J, Owen J H G, Miki K *J. Phys. Condens. Matter* **24** 095005 (2012)
74. Zandvliet H J W *Phys. Rep.* **388** 1 (2003)
75. Oncel N, Nicholls D *J. Phys. Condens. Matter* **25** 014010 (2012)
76. Hamers R J, Tromp R M, Demuth J E *Phys. Rev. B* **34** 5343 (1986)
77. Li Y et al. *Phys. Rev. B* **56** 12539 (1997)
78. Ferrando R, Hontinfinde F, Levi A C *Phys. Rev. B* **56** R4406 (1997)
79. Stepanyuk O V et al. *Phys. Rev. B* **78** 113406 (2008)
80. Stepanyuk O V et al. *Phys. Rev. B* **79** 155410 (2009)
81. Mottet C et al. *Surf. Sci.* **417** 220 (1998)
82. Amar J G, Popescu M N, Family F *Phys. Rev. Lett.* **86** 3092 (2001)
83. Syromyatnikov A G, Saletsky A M, Klavsyuk A L *JETP Lett.* **107** 766 (2018); *Pis'ma Zh. Eksp. Teor. Fiz.* 107 794 (2018)
84. Ramadan A, Picaud F, Ramseyer C *Surf. Sci.* **604** 1576 (2010)
85. Tokar V I, Dreyssé H *Surf. Sci.* **637–638** 116 (2015)
86. Albao M A et al. *Phys. Rev. B* **72** 035426 (2005)
87. Stinchcombe R B, Aarão Reis F D A *Phys. Rev. B* **77** 035406 (2008)
88. Shi F, Shim Y, Amar J G *Phys. Rev. E* **79** 011602 (2009)
89. Javorský J et al. *Phys. Rev. B* **79** 165424 (2009)
90. Albia J R, Albao M A *Phys. Rev. E* **95** 042802 (2017)
91. González D L, Camargo M, Sánchez J A *Phys. Rev. E* **97** 052802 (2018)
92. Brune H *Surf. Sci. Rep.* **31** 125 (1998)
93. Evans J W, Thiel P A, Bartelt M C *Surf. Sci. Rep.* **61** 1 (2006)
94. Dieterich W, Einax M, Maass P *Eur. Phys. J. Special Topics* **161** 151 (2008)
95. Einax M, Dieterich W, Maass P *Rev. Mod. Phys.* **85** 921 (2013)
96. Vicsek T, Family F *Phys. Rev. Lett.* **52** 1669 (1984)
97. Bartelt M C et al. *Phys. Rev. Lett.* **81** 1901 (1998)
98. Bartelt M C et al. *Phys. Rev. B* **59** 3125 (1999)
99. Bartelt M C, Evans J W *Phys. Rev. B* **54** R17359 (1996)

100. Venables J A *Philos. Mag.* **27** 697 (1973)
101. Venables J A, Spiller G D T, Hanbucken M *Rep. Prog. Phys.* **47** 399 (1984)
102. Stoyanov S, Kashchiev D *Current Topics Mater. Sci.* **7** 69 (1981)
103. Walton D *J. Chem. Phys.* **37** 2182 (1962)
104. Li M, Bartelt M C, Evans J W *Phys. Rev. B* **68** 121401 (2003)
105. Li M, Evans J W *Surf. Sci.* **546** 127 (2003)
106. Li M, Evans J W *Multiscale Model. Simul.* **3** 629 (2005)
107. Dubrovskii V G, Berdnikov Yu S, Sokolova Zh V *Tech. Phys. Lett.* **41** 242 (2015); *Pis'ma Zh. Teor. Fiz.* **41** (5) 74 (2015)
108. Dubrovskii V G, Sibirev N V *Phys. Rev. E* **91** 042408 (2015)
109. Evans J W, Bartelt M C *Phys. Rev. B* **63** 235408 (2001)
110. Körner M, Einax M, Maass P *Phys. Rev. B* **86** 085403 (2012)
111. Gibou F G et al. *Phys. Rev. B* **63** 115401 (2001)
112. Gibou F, Ratsch C, Caflisch R *Phys. Rev. B* **67** 155403 (2003)
113. Dubrovskii V G *Nucleation Theory and Growth of Nanostructures* (Berlin: Springer-Verlag, 2014)
114. Berdnikov Y, Dubrovskii V G *J. Phys. Conf. Ser.* **541** 012089 (2014)
115. Tokar V I, Dreyssé H *Phys. Rev. B* **74** 115414 (2006)
116. Amar J G, Popescu M N *Phys. Rev. B* **69** 033401 (2004)
117. Brune H et al. *Phys. Rev. B* **60** 5991 (1999)
118. Han Y et al. *Phys. Rev. B* **87** 155420 (2013)
119. Hamers R J, Köhler U K *J. Vac. Sci. Technol. A* **7** 2854 (1989)
120. Vanpoucke D E P *J. Phys. Condens. Matter* **26** 133001 (2014)
121. Lukanov B R et al. *Phys. Rev. B* **89** 155319 (2014)
122. Owen J H G et al. *Phys. Rev. Lett.* **88** 226104 (2002)
123. Vanpoucke D E P, Brocks G *Phys. Rev. B* **81** 085410 (2010)
124. Song I et al. *New J. Phys.* **11** 063034 (2009)
125. Koczorowski W et al. *Phys. Rev. B* **91** 235319 (2015)
126. Schwingenschlögl U, Schuster C *Eur. Phys. J. B* **60** 409 (2007)
127. Gurlu O et al. *Phys. Rev. B* **70** 085312 (2004)
128. Pick V et al. *J. Phys. Condens. Matter* **19** 446001 (2007)
129. Syromyatnikov A G et al. *Mater. Lett.* **179** 69 (2016)
130. Kohn W *Rev. Mod. Phys.* **71** 1253 (1999); *Usp. Fiz. Nauk* **172** 336 (2002)
131. Zaki N et al. *Phys. Rev. B* **89** 205427 (2014)
132. Kolesnikov S V, Klavsyuk A L, Saletsky A M *Surf. Sci.* **612** 48 (2013)
133. Schüler M et al. *New J. Phys.* **19** 073016 (2017)
134. Néel N et al. *Phys. Rev. Lett.* **107** 106804 (2011)
135. Hansen O et al. *Phys. Rev. Lett.* **81** 5572 (1998)
136. Binnig G, Rohrer H *Angew. Chem. Int. Ed. Engl.* **26** 606 (1987); *Usp. Fiz. Nauk* **154** 261 (1988)
137. Metropolis N et al. *J. Chem. Phys.* **21** 1087 (1953)
138. Ising E *Z. Phys.* **31** 253 (1925)
139. Limot L et al. *Phys. Rev. Lett.* **94** 036805 (2005)
140. Sánchez O et al. *Phys. Rev. B* **52** 7894 (1995)
141. Hansmann M et al. *Phys. Rev. B* **67** 121409 (2003)
142. Ignatiev P A et al. *Phys. Rev. B* **75** 155428 (2007)
143. Shiraki S et al. *Phys. Rev. Lett.* **92** 096102 (2004)
144. Olsson F E et al. *Phys. Rev. Lett.* **93** 206803 (2004)
145. Davydov S Yu, Troshin S V *Phys. Solid State* **49** 1583 (2007); *Fiz. Tverd. Tela* **49** 1508 (2007)
146. Anderson P W *Phys. Rev.* **124** 41 (1961)
147. Newns D M *Phys. Rev.* **178** 1123 (1969)
148. Borisov A G, Kazansky A K, Gauyacq J P *Phys. Rev. B* **59** 10935 (1999)
149. Li J et al. *Phys. Rev. Lett.* **81** 4464 (1998)
150. Stepanyuk V S et al. *Phys. Rev. B* **72** 153407 (2005)
151. Lazarovits B, Szunyogh L, Weinberger P *Phys. Rev. B* **73** 045430 (2006)
152. Lounis S et al. *Phys. Rev. B* **73** 195421 (2006)
153. Nilius N, Wallis T M, Ho W *Science* **297** 1853 (2002)
154. Rashba E I *Fiz. Tverd. Tela* **2** 1224 (1960)
155. Bychkov Yu A, Rashba E I *JETP Lett.* **39** 78 (1984); *Pis'ma Zh. Eksp. Teor. Fiz.* **39** 66 (1984)
156. Bychkov Y A, Rashba E I *J. Phys. C* **17** 6039 (1984)
157. Dolcini F, Rossi F *Phys. Rev. B* **98** 045436 (2018)
158. Wójcik P et al. *J. Appl. Phys.* **115** 104310 (2014)
159. Nitta J et al. *Phys. Rev. Lett.* **78** 1335 (1997)
160. Barke I et al. *Phys. Rev. Lett.* **97** 226405 (2006)
161. Kopciuszyński M et al. *Sci. Rep.* **7** (1) (2017)
162. Nakamura T et al. *Phys. Rev. B* **98** 075431 (2018)
163. Takayama A et al. *Phys. Rev. Lett.* **114** 066402 (2015)
164. Governale M, Zülicke U *Phys. Rev. B* **66** 073311 (2002)
165. Yoh K et al., in *70th Device Research Conf., IEEE2012*
166. Landauer R *Philos. Mag.* **21** 863 (1970)
167. Büttiker M *Phys. Rev. Lett.* **57** 1761 (1986)
168. Koeik Z, Sakr M R *Physica E* **74** 527 (2015)
169. Sander D *J. Phys. Condens. Matter* **16** R603 (2004)
170. Enders A, Skomski R, Honolka J *J. Phys. Condens. Matter* **22** 433001 (2010)
171. Wang H et al. *Nano* **06** (01) 1 (2011)
172. Barth J V, Costantini G, Kern K *Nature* **437** 671 (2005)
173. Gambardella P *Science* **300** 1130 (2003)
174. Brune H, Gambardella P *Surf. Sci.* **603** 1812 (2009)
175. Balashov T et al. *Phys. Rev. Lett.* **102** 257203 (2009)
176. Bansmann J et al. *Surf. Sci. Rep.* **56** 189 (2005)
177. Shen J et al. *J. Phys. Condens. Matter* **15** R1 (2002)
178. Gambardella P et al. *Phys. Rev. Lett.* **93** 077203 (2004)
179. Dupé B et al. *New J. Phys.* **17** 023014 (2015)
180. Otte F, Ferriani P, Heinze S *Phys. Rev. B* **89** 205426 (2014)
181. Félix-Medina R, Dorantes-Dávila J, Pastor G M *New J. Phys.* **4** 100 (2002)
182. Martins M, Wurth W *J. Phys. Condens. Matter* **28** 503002 (2016)
183. Pick S et al. *Phys. Rev. B* **70** 224419 (2004)
184. Klavsyuk A L, Kolesnikov S V, Saletsky A M *JETP Lett.* **99** 646 (2014); *Pis'ma Zh. Eksp. Teor. Fiz.* **99** 750 (2014)
185. Gomonay O et al. *Nat. Phys.* **14** 213 (2018)
186. Baltz V et al. *Rev. Mod. Phys.* **90** 015005 (2018)
187. Gomonay E V, Loktev V M *Low Temp. Phys.* **40** 17 (2014)
188. Jungwirth T et al. *Nat. Nanotechnol.* **11** 231 (2016)
189. Yan S et al. *Nat. Nanotechnol.* **10** 40 (2014)
190. Etzkorn M et al. *Phys. Rev. B* **92** 184406 (2015)
191. Ferrón A, Lado J L, Fernández-Rossier J *Phys. Rev. B* **92** 174407 (2015)
192. Choi D J et al. *Phys. Rev. B* **94** 085406 (2016)
193. Urdaniz M C, Barral M A, Llois A M *Phys. Rev. B* **86** 245416 (2012)
194. Tao K et al. *Phys. Chem. Chem. Phys.* **17** 26302 (2015)
195. Urdaniz M C et al. *Phys. Rev. B* **90** 195423 (2014)
196. Udvardi L et al. *Phys. Rev. B* **68** 104436 (2003)
197. Hermenau J et al. *Nat. Commun.* **10** 2565 (2019)
198. Dzyaloshinsky I *J. Phys. Chem. Solids* **4** 241 (1958)
199. Moriya T *Phys. Rev.* **120** 91 (1960)
200. Menzel M et al. *Phys. Rev. Lett.* **108** 197204 (2012)
201. Schweflinghaus B et al. *Phys. Rev. B* **94** 024403 (2016)
202. Tao K, Polyakov O P, Stepanyuk V S *Phys. Rev. B* **93** 161412 (2016)
203. Ebert H, Ködderitzsch D, Minár J *Rep. Prog. Phys.* **74** 096501 (2011)
204. Lazarovits B et al. *Phys. Rev. B* **68** 024433 (2003)
205. Bruno P *Phys. Rev. B* **39** 865 (1989)
206. Mermin N D, Wagner H *Phys. Rev. Lett.* **17** 1133 (1966)
207. Choi D J et al. *Rev. Mod. Phys.* **91** 041001 (2019)
208. Bose S *Phys. Rev. Lett.* **91** 207901 (2003)
209. Verma H et al. *Europhys. Lett.* **119** 30001 (2017)
210. Barabanenkov Yu N, Nikitov S A, Barabanenkov M Yu *Phys. Usp.* **62** 82 (2019); *Usp. Fiz. Nauk* **189** 85 (2019)
211. Gauyacq J P, Lorente N *J. Phys. Condens. Matter* **27** 455301 (2015)
212. Bryant B et al. *Phys. Rev. Lett.* **111** 127203 (2013)
213. Cohen-Tannoudji C, Dupont-Roc J, Grynberg G *Atom-Photon Interactions: Basic Process and Applications* (New York: Wiley, 1998)
214. Shishkov V Yu et al. *Phys. Usp.* **62** 510 (2019); *Usp. Fiz. Nauk* **189** 544 (2019)
215. Gauyacq J P, Lorente N *Surf. Sci.* **630** 325 (2014)
216. Landau L, Lifshitz E, in *Perspectives in Theoretical Physics: the Collected Papers of E.M. Lifshitz* (Ed. L P Pitaevskii) (Oxford: Pergamon Press, 1992) pp. 51 – 65
217. Lifshitz E M, Pitaevskii L P *Statistical Physics* Vol. 2 *Theory of the Condensed State* (Oxford: Butterworth-Heinemann, 1980); Translated into Russian: *Statisticheskaya Fizika* Vol. 2 *Theoriya Kondensirovannogo Sostoyaniya* (Moscow: Fizmatlit, 2004)
218. Li Y, Liu B G *Phys. Rev. B* **73** 174418 (2006)
219. Glauber R J *J. Math. Phys.* **4** 294 (1963)
220. Li J, Liu B G *J. Magn. Magn. Mater.* **378** 186 (2015)
221. Smirnov A S et al. *New J. Phys.* **11** 063004 (2009)

222. Li Y, Liu B G *Phys. Rev. Lett.* **96** 217201 (2006)
223. He L, Kong D, Chen C *J. Phys. Condens. Matter* **19** 446207 (2007)
224. Tsysar K M, Kolesnikov S V, Saletsky A M *Chinese Phys. B* **24** 097302 (2015)
225. Kolesnikov S V, Tsysar K M, Saletsky A M *Phys. Solid State* **57** 1513 (2015); *Fiz. Tverd. Tela* **57** 1492 (2015)
226. Tsysar K M et al. *Mod. Phys. Lett. B* **31** 1750142 (2017)
227. Kolesnikov S V *JETP Lett.* **103** 588 (2016); *Pis'ma Zh. Eksp. Teor. Fiz.* **103** 668 (2016)
228. Kolesnikov S V, Kolesnikova I N *J. Exp. Theor. Phys.* **125** 644 (2017); *Zh. Eksp. Teor. Fiz.* **152** 759 (2017)
229. Puchala B, Falk M L, Garikipati K *J. Chem. Phys.* **132** 134104 (2010)
230. Kolesnikov S V et al. *Mat. Modelirovanie* **30** (2) 48 (2018)
231. Kolesnikov S V, Kolesnikova I N *IEEE Magn. Lett.* **10** 2509105 (2019)
232. Kolesnikov S V, Kolesnikova I N *Phys. Rev. B* **100** 224424 (2019)